Toward Scalable Fabrication of Stable Metal Halide Perovskite Solar Cells Through Inkjet Printing and Antisolvent Engineering of $CH_3NH_3PbI_3$-Polymer Films

by

Marc Joseph Migliozzi

B.S. Mechanical Engineering, University of Akron, 2020

Submitted to the Graduate Faculty of the

Swanson School of Engineering in partial fulfillment

of the requirements for the degree of

Master of Science in Mechanical Engineering

University of Pittsburgh

2022

UNIVERSITY OF PITTSBURGH

SWANSON SCHOOL OF ENGINEERING

This thesis was presented

by

Marc Joseph Migliozzi

It was defended on

March 21, 2022

and approved by

Jung-Kun Lee, Ph.D., Professor

Department of Mechanical Engineering and Materials Science

Tony Kerzmann, Ph.D., Associate Professor

Department of Mechanical Engineering and Materials Science

Markus Chmielus, Ph.D., Associate Professor

Department of Mechanical Engineering and Materials Science

Thesis Advisor: Jung-Kun Lee, Ph.D., Professor,

Department of Mechanical Engineering and Materials Science

Toward Scalable Fabrication of Stable Metal Halide Perovskite Solar Cells Through Inkjet Printing and Antisolvent Engineering of $CH_3NH_3PbI_3$-Polymer Films

Marc Joseph Migliozzi, M.S.

University of Pittsburgh, 2022

Due to rapid progress in recent years, the power conversion efficiencies (PCEs) of metal halide perovskite solar cells (PSCs) have become comparable to that of standard crystalline silicon (c-Si) solar cells. Yet, the reliance on small-scale perovskite deposition techniques, and perovskite's inherent instability, have slowed the commercialization of this technology.

In this thesis, I have studied a scalable fabrication process for PSCs, which is based on inkjet printing and antisolvent bathing. It is found that piezoelectric waveform parameters, drop spacing, substrate surface energy, and ink rheology all affect the dynamic behavior of the deposited ink on the substrate. This research has established relationships between the degree of droplet spreading and the final morphology of the crystallized perovskite are made. The highly coordinating DMSO solvent is found to form the important $MAI \cdot PbI_2 \cdot DMSO$ intermediate phase easily in an antisolvent in which it is not miscible. The grain size, which is related to the density of nucleation sites, can be controlled by adjusting the antisolvent bathing duration and number of passes during inkjet printing.

In addition, I have demonstrated that the stability and performance of inkjet printed PSCs can be enhanced by adding small amounts of polyvinylpyrrolidone (PVP) directly into the film. Fourier transform infrared spectroscopy (FTIR) analysis suggested the formation of Lewis acid-base adducts between the oxygen in PVP and the dangling Pb^{2+} ions present in grain boundaries. Stability, which is characterized in terms of PCE over time, as well as the ratio of PbI_2 to

characteristic perovskite x-ray diffraction peaks, was found to be enhanced, which is credited to the PVP-induced inter-grain cross-linking effects. The champion device from the proposed approach exhibited a PCE of 16.2% and retained 73% of its initial PCE over a 30-day period in ambient conditions.

Table of Contents

List of Tables

List of Figures

Acknowledgment

I would first like to thank my advisor, Dr. Jung-Kun Lee, for his continuous guidance and support. I am so grateful to have had the opportunity to work and learn from an advisor that cares so much for his students.

I would also like to thank my committee members, Dr. Tony Kerzmann and Dr. Markus Chmielus, who have been instrumental in the development of this project. I appreciate your insights, critiques, and valuable time.

To my lab-mates; Seongha, Jun, Joe, Yulin, Sumin, Anqi, and Vishal, your insights and experience have been invaluable to this project, and I am very thankful to have made such great friends who made coming into the laboratory every day so much fun. Thank you for these unforgettable two years.

My family has been an incredible motivation. John, Jeffrey, Samantha, Evan; thank you for believing in me. The best part about moving back to Pittsburgh was getting to spend more time with each of you. Mom, thank you for always showing excitement in my research. Your unwavering support and encouragement motivate me every day. Dad, thank you for being my role model. You have taught me so much about the world, as well as what is important in life. I am constantly inspired by your thirst for knowledge, selflessness, and empathy for others.

Lastly, to all my friends, new and old, thank you for making these past two years so enjoyable.

1.0 Introduction

Since their realization in 2009, hybrid organic-inorganic metal halide perovskite solar cells (PSC) have developed at an unprecedented rate. Recent PSC power conversion efficiencies (PCE) are now competitive with silicon-based cells, all the while boasting additional attributes such as translucence, flexibility, and relatively low cost of fabrication. Up until recently, PSCs have almost exclusively relied on spin coating for perovskite deposition and solvent removal. Spin coating is a reliable means of deposition, but it is wasteful, and cannot be scaled up for high throughput processing. Furthermore, the instability of perovskite thin films threatens the operating lifetime of perovskite modules.

A necessary task in the development of PSCs is to upscale traditional deposition methods so that large-scale devices can be processed in a cost-effective manner. So far, spin coating has been the dominant method of perovskite precursor solution deposition. Spin coating is a proven method for thin film deposition but is wasteful and cannot deposit solutions over large areas. Furthermore, the subsequent solvent washing step, which induces the important $MAI \cdot PbI_2 \cdot DMSO$ intermediate phase, is also typically reliant on the use of a spin coater. Research in recent years has turned to alternative deposition methods such as inkjet printing, which is advantageous due to its exceptional control over the deposited area, high-throughput capabilities, and low material waste. Even still, most inkjet printing studies have relied on low vacuum pressure to remove solvents effectively. [1]–[5] Vacuum chambers are not compatible with scalable processing, so other solvent removal techniques must be explored. Antisolvent bathing is an alternative method for solvent removal which could be paired with inkjet printing for scalable fabrication. There have been a few promising reports of antisolvent bathing for perovskite films deposited via slot die casting and gravure printing [7][8].

The instability of perovskite films must also be addressed before this technology can become commercialized. Perovskite films are susceptible to degradation when exposed to high temperatures or ambient environmental conditions. Humidity and oxygen are particularly detrimental to perovskite films. These contaminants can travel through grain boundaries in polycrystalline perovskite, working from the edges of the film and traveling inward. Researchers have taken multiple approaches to this addressing this issue. In-situ polymer additives have been shown to enhance the stability of the film through several mechanisms related to grain boundary passivation. [8]–[13] The driving mechanism is commonly cited as Lewis acid-base adducts that can be formed between common polymers and dangling bonds of Pb ions, which are found in grain boundaries. To the best of the author’s knowledge, there are no reports of inkjet printing followed by antisolvent bathing for perovskite solar cell fabrication. Furthermore, there are no demonstrations of inkjet printing perovskite-polymer precursor inks.

Herein, I report one-step inkjet-printed and antisolvent bathed perovskite-polymer solar cells with a champion efficiency of 16.2 % and enhanced stability compared to reference solar cells. It was found that the precursor solution rheology, printing parameters, and substrate surface treatment largely affect the printability of the precursor solution, the spreading of the ink, and the morphology of the film. Antisolvent bath compositions were investigated to optimize the process. Diethyl ether (DE) was found to most aptly complement the antisolvent bathing process, which is likely due to its ability to induce the intermediate phase, thanks to its immiscibility with the coordinating solvent dimethyl sulfoxide (DMSO). A DMSO:DMF volumetric ratio of 1:6.5 was optimized to preserve the film during printing. Multiple passes of inkjet printing were found to enhance grain size, possibly to do the redissolving of seed crystals, decreasing the overall density of nucleation sites in the film before antisolvent bathing.

2.0 Background

2.1 Solar Energy

As the world's population grows, so too will our consumption of energy. Projections show that global energy consumption between the years 2018 and 2050 will increase by almost 50%. [14] There is overwhelming consensus among the scientific community that greenhouse gas emissions are causing the global climate to change at an alarming rate. [15] As seen in Fig. 1, just over 73% of the 49.4 billion tonnes of greenhouse gasses that were released in 2016 were from the energy sector. [16] The urgent integration of clean and renewable energy is an imperative step in the fight against climate change. As countries around the world commit to drastically reduce emissions in the coming decades, energy generation technology must be innovated to make the transition as seamless and cost-effective as possible.

Renewable energy is defined as energy that comes from a source that cannot be depleted. Common examples are wind, hydroelectric, and solar. Of these renewable energy sources, solar is particularly attractive, as solar radiation is abundant and reliable. Two main forms of capturing solar energy exist: solar thermal systems and photovoltaic (PV) solar cells. Solar thermal systems use mirrors to concentrate thermal energy into a region where a transfer fluid such as synthetic oil can efficiently transfer the heat to convert it to electricity. Solar PV describes the process of using semiconducting materials to directly convert sunlight into electricity. Solar thermal systems are large and considerably less practical than solar PV technology.

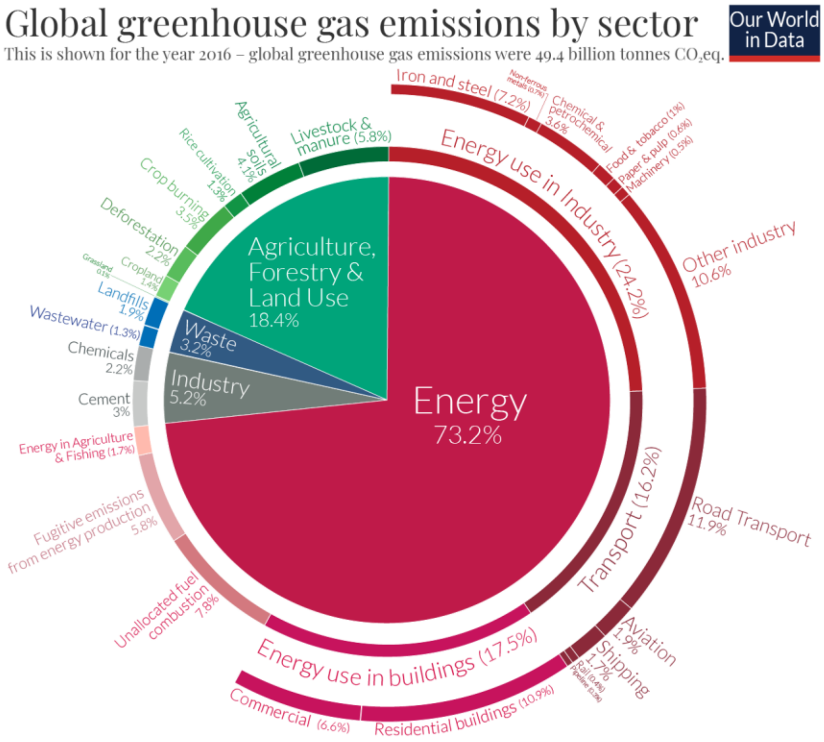

Figure 1. Global Greenhouse Gas Emissions by Sector. Figure from Our World in Data. Data from Climate Watch, the World Resources Institute (WRI). [16]

As for PV technology, silicon-based solar cells currently dominate the market. They are efficient, reliable, and are usually operational for over 20 years. Yet, despite the falling cost of solar energy, silicon (Si) solar cells are cost and energy exhaustive to process relative to new advanced materials. Furthermore, Si solar modules are generally heavy, bulky, and not easily integrated into new or existing infrastructure. To make solar energy more accessible, new semiconducting materials have been explored as alternatives to silicon. There have been many promising alternatives such as gallium arsenide, copper indium gallium selenide, and metal halide perovskites. New research in the field emphasizes materials that are compatible with low-cost, scalable processing techniques. Thin film and semi-transparent solar cells are also of significant interest, as these attributes open doors for unique applications of PV technology.

2.1.1 Working Principles of Photovoltaic Cells

The photovoltaic effect, which describes the process in which semiconductor devices can generate electric current under the illumination of solar radiation, is the basic operating principle for solar cells. Solar cell active layers are made from semiconductors, which are an intermediate class of materials between conductors and insulators. Semiconductors are unique in that their bandgap energy is not large enough to completely insulate; yet, an energy difference still exists between the atom's valence and conduction bands. Certain materials such as Si have a bandgap energy that electrons can overcome with photon energy from the sun. Semiconductors can also be doped, which means adding elements with one more – or one less – valence electron. In the case of Si, a group IV element, doping with a group V element would provide extra unbonded electrons that would give the material an overall negative charge. This is called an n-type semiconductor. P-type semiconductors have additional atoms of a group III element, so the lack of electrons with respect to a group IV semiconductor gives the p-type a net positive charge.

When the two doped semiconductors are joined, a p-n junction is formed between them. Due to the proximity of the two oppositely charged materials, nearby electrons and holes recombine and cancel each other out, due to diffusion. Eventually, a positive charge will build on the n-side, and a negative charge will build on the p-side, due to dopant ions' fixed position in the crystal lattice. The result is an electric field. This area between the two doped sides is called a depletion zone. Current can be harvested using this array, as incoming solar radiation in the form of photons excites valence electrons in the p-n junction from the valence to the conduction band, leaving behind holes. These free charge carriers drift to their respective sides of the junction, under the direction of the electric field. The accumulation of these charges creates an electrical potential across the depletion region. The electrons' desire to recombine with holes is what can be captured as electricity, and this is done simply by completing the circuit between the positive and negative sides of the device.

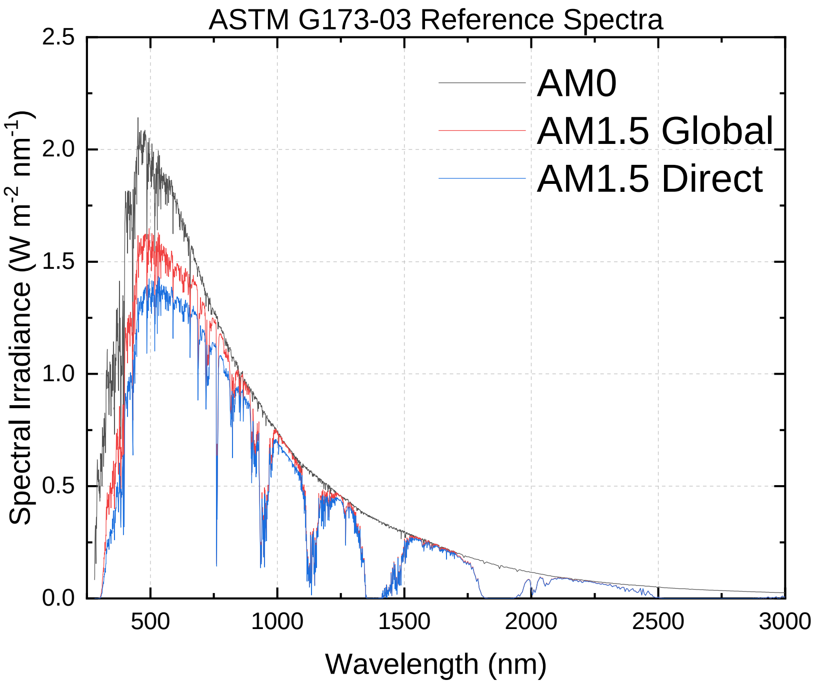

Figure 2. Incident Solar Spectrum. Data from The American Society for Testing and Materials (ASTM). [17]

Since the bandgap dictates how much energy is required to free an electron from the valence band, it is a good indication of how suitable the material is for light-harvesting applications. Materials for outdoor solar cell applications should have a bandgap that can effectively use light that is abundant on earth. The bang gap of crystalline silicon is 1.12 eV. Converting this to wavelength gives a value of 1100 nanometers (nm), which falls well within the spectrum of blackbody radiation emitted from the sun, as seen in Fig. 2.

2.1.2 Performance Analysis of Solar Cells

The quality of a solar cell can be determined from the generation of a current-voltage (IV) curve, which shows how much current is generated as a function of applied voltage across the device. A sample IV curve is seen in Fig. 3. Current is often expressed as current density (J_{sc}), which is simply the amount of current generated per unit of area. The IV curve endpoints are called the short circuit current (I_{sc}) and the open-circuit voltage (V_{oc}). Short circuit current is the maximum current that can flow through the device when the potential across the solar cell is zero. V_{oc} is the maximum voltage when there is no current flowing through the device.

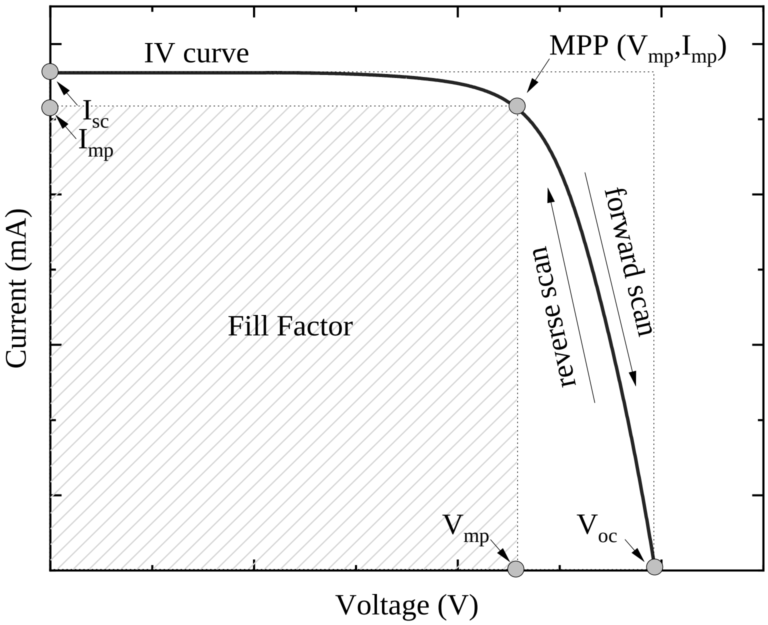

Figure 3. The IV Curve

Typically, a low I_{sc} indicates the presence of series resistance, which can arise from contact resistance due to poor layer-to-layer interfacial contact. A low V_{oc} is caused by low shunt resistance across the device, meaning that the path of least resistance for electrons is not the intended one. This is often the case when pinholes or impurities are prevalent in the active layer of the solar cell, which creates shortcuts through the device layers. Electrons and holes can travel through these pathways and inhibit the device's ability to build up potential.

Also seen in Fig. 3 are the fill factor (FF) and maximum power point (MPP). The FF describes the squareness of the curve and represents the largest area that can be drawn under the IV curve. The FF also indicates the location of the MPP. The MPP shows the conditions in which the maximum power can be drawn from a solar cell, which can be thought of as a compromise between current and voltage. FF is expressed in terms of percentage, and its formula can be found in Eq. 1.

$$FF = \frac{V_{mp} \cdot I_{mp}}{V_{oc} \cdot I_{sc}} = \frac{MPP}{V_{oc} \cdot I_{sc}} \tag{2-1}$$

The IV curve is usually generated by taking a reverse scan, from high to low voltage. To further analysis of a solar cell, forward-scanned curves must also be produced, to check for hysteresis. JV hysteresis is a phenomenon that occurs when the solar cell IV curve is dependent on the direction of the scan. This hysteresis can often be attributed to poor interfacial contact between layers, which can lead to charge accumulation and reduce the internal electric field which is responsible for the generation of photocurrent. [18] [19] Interfacial contact can also deplete the capacitance of the device capacitance. [19] Other origins include charge carrier trapping and band bending. [19] If there is large hysteresis seen in the forward and reverse scan directions, then a single scan direction may be an overestimate of the efficiency of the device. Thus, the forward and reverse scan directions are usually simultaneously reported in literature, to affirm the capabilities of the solar cell.

The power conversion efficiency (PCE) is the principal indication of the quality of a solar cell, as it considers all the aforementioned parameters. The PCE describes the ratio of energy generated from the solar cell to the energy that falls onto the solar cell (P_{in}). It can be mathematically expressed as seen in Eq. 2.

$$\eta = \frac{J_{sc} \times V_{oc} \times FF}{P_{in}} \tag{2-2}$$

Incident photon to charge carrier efficiency (IPCE), sometimes referred to as quantum efficiency, is another important value for the analysis of a solar cell. IPCE is defined as the ratio of carriers collected by the solar cell to the number of photons of a particular wavelength, as seen in Eq. 3. IPCE is useful to examine which wavelengths are absorbed, and which ones are not. Deficits in the curve can indicate that certain wavelengths may be more likely to be reflected by the material. For example, higher energy wavelengths, such as blue and ultraviolet (UV) radiation, are often not efficiently converted into current due to their smaller penetration depth, and thus increased vulnerability to surface recombination. The curve falls to zero at energies below the bandgap value. Both the PCE and IPCE assume the air mass 1.5 Global (AM1.5G) condition, which is representative of the average solar irradiation on earth.

$$IPCE = \frac{electrons\ generated}{incident\ photons} = \frac{1240 \times J_{sc}}{\lambda \times P_{in}} \times 100 \tag{2-3}$$

A typical IPCE curve for a solar cell can be found in Fig. 4. A typical PV cell is most efficient at absorbing wavelengths between blue and red light. At the higher wavelengths, the IPCE approaches zero due to surface recombination at the front of the device, which is a side effect of this wavelength’s relatively short penetration depth. At the surface, there tends to be a higher concentration of defects such as dangling bonds, which induces recombination, and thus reduces the number of charge carriers that can be collected for current. At wavelengths approaching the bandgap energy, the IPCE curve decreases due to surface recombination at the rear of the device. This is due to the longer penetration depths of these wavelengths, which in a similar fashion, induces recombination at the surface. The IPCE falls to zero at energies below the bandgap energy, as the incident radiation does not carry enough energy to excite electrons and generate photocurrent.

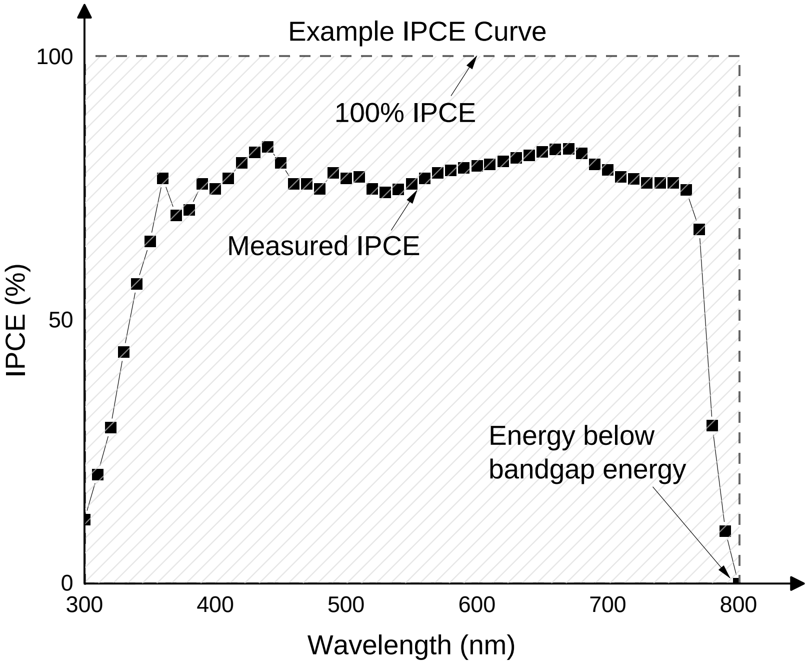

Figure 4. The IPCE curve

2.2 Perovskite Solar Cells

2.2.1 Perovskite as a Light-Harvesting Material

The mineral of perovskite was discovered in the Ural Mountains of Russia by Alexander Kämmerer in 1839, and it was later identified by German mineralogist Gustav Rose. [20] The mineral was later named after Russian mineralogist Lev Perovski. The first known analog of perovskite was calcium titanate, but it is the crystal structure, commonly described as ABX_3 that defines a perovskite. A and B are organic and metal cation sites, respectively, and X is an anion. The crystal structure of perovskite is seen in Fig. 5. Generally, the popular perovskite analog $CH_3NH_3PbI_3$ has a stable tetragonal phase at low temperatures but will undergo phase change at 54°C to the cubic structure. [21][22] This phase change is not thought to have a significant impact on its light-harvesting abilities. [22] $CH_3NH_3PbI_3$ perovskite, commonly expressed as $MAPbI_3$, has a bandgap of approximately 1.55 eV, which translates to a photon wavelength of about 800 nanometers. Considering the high abundance of electromagnetic radiation that falls onto earth in this range, the perovskite bandgap is compatible for light-harvesting applications. Furthermore, because perovskite only describes a crystal structure, different cations and anions can be substituted into A and X sites, respectively, to chemically alter several properties of perovskite. These different chemical analogs open the door for bandgap tuning, which can potentially lower the bandgap to energies that align with higher theoretical maximum efficiencies as given by the Shockley-Queisser limit. Bandgap tuning can also be useful for multijunction solar cells, where each layer is responsible for a different portion of the electromagnetic spectrum.

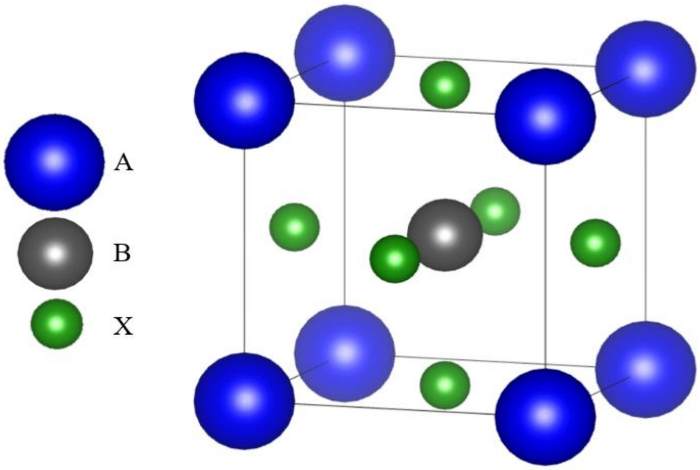

Figure 5. Crystal Structure of Perovskite

Perovskites are often described as being defect tolerant, which allows for long carrier diffusion lengths and carrier lifetime. Defects, which arise from sources such as structural disorder or environmental exposure, form energy states around the site of the defect. [23] These defects can be harmful if they occupy an energy level in between the valence and conduction bands. Although perovskite has a relatively low defect formation energy, many of its defects are considered inert, or benign, due to its preferred formation in shallow states. [23] [24] Shallow states are defect states near the conduction or valence bands, while deep states manifest towards the center of the bandgap gap. Due to their location in the band structure, shallow state defects often behave as dopants, while deep states can cause recombination and emission of potentially damaging energy. [25]

Perovskites also possess excellent absorbance properties. Compared to other common semiconductors, the absorbance coefficient of perovskite is remarkably stable across energies higher than its own bandgap. [24] This is partly thanks to the direct bandgap of perovskites, meaning that the valence and conduction bands align at the same value of momentum. Silicon has an indirect bandgap, so the valence and conduction band align at different values of momentum, and extra lattice vibrational phonon energy is needed to excite the electron to the conduction band. Consequently, Si active layers must be thick to offset their poor absorption.

2.2.2 Working Principles of Perovskite Solar Cells

The working principles of perovskite solar cells are like that of traditional silicon solar cells. The distinguishable difference lies in the architecture of the devices. Where silicon devices have a simple p-n junction formed at the interface of two oppositely doped silicon layers, PSCs have an extra intrinsic layer, giving the device an architecture of n-i-p or p-i-n. The “i" represents the intrinsic perovskite layer, and the n and p represent the negative and positively doped sides.

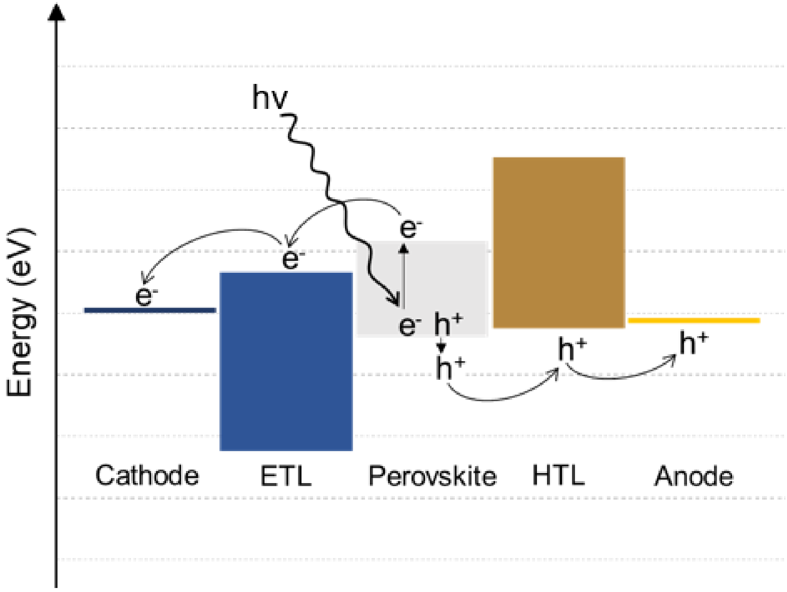

Figure 6. Energy Band Diagram of a Perovskite Solar Cell

In the n-i-p configuration, light travels through the electron transport layer (ETL), before being absorbed into the perovskite. In the p-i-n configuration, light first travels through the hole transport layer. N-i-p is the most common architecture in literature, and it generally relies on the transparent TiO_2 ETL for efficient electron extraction. There are two standard n-i-p models: mesoporous and planer. The planer model has one ETL layer of compact or blocking layer (bl) TiO_2. The mesoporous model relies on an additional mesoporous TiO_2 (m-TiO_2) layer on top of the bl-TiO_2. The purpose of the mesoporous layer is to act as a scaffold for the perovskite, which increases the surface area between the two layers and enhances electron extraction. The improved interfacial contact has also been shown to reduce JV hysteresis. [26] In a p-i-n configuration, light travels through the hole transport layer (HTL). There is no solid consensus on which architecture is superior, and the choice between n-i-p and p-i-n is usually determined by the transport material selection. This project will focus on the n-i-p configuration.

In a PSC, perovskite is the primary light-harvesting material, meaning that when light is absorbed into it, electron-hole pairs are created. The alignment of the band energies, as seen in Fig. 6, acts as an energy barrier for electrons and helps drive the charge separation of the electron-hole pairs to their respective transport layers. The electrons move to the TiO_2 ETL layer, which is intrinsically n-type. The holes move up to the p-type HTL, which is commonly made from 2′,7,7′-tetrakis-(N,N-di-p-methoxyphenylamino)9,9′-spirobifluorene (Spiro-OMeTAD) doped with lithium bis(trifluoromethane sulfonyl)imide (Li salt).

2.2.3 Development of Perovskite Solar Cells

The first report of perovskite solar cells came in 2009 when Miyasaka et al. reported $MAPbI_3$-based devices with a power conversion efficiency of 3.8% [27] These cells employed the use of a liquid electrolyte between electrodes, but it dissolved the perovskite and resulted in a very short operating lifetime. Breakthroughs came in 2012 with the realization of solid-state Spiro-OMeTAD as an effective means of extracting holes from the perovskite without the need for a corrosive liquid electrolyte. [28][29] As seen in Fig. 7, perovskite technology has since made impressive advancements since 2009.

The early to mid-2010s were marked by optimization of processing techniques and device architecture, which greatly improved the efficiencies of devices made at that time. Understandably, the primary focus in the field at the time was improving the power conversion efficiency, and problems such as scalability and inherent stability were largely looked over. As PCEs approaching silicon-based solar cells started to emerge, the focus began to shift from increasing efficiency to increasing the stability and scalability of PSCs. Existing thin-film application methods such as slot-die casting and inkjet printing are now being realized for scalable perovskite deposition. New perovskite analogs, and polymer additives, are commonly tested for enhanced stability and efficiency. Recently, H. Min et al. fabricated an α-formamidinium lead triiodide-based PSC with a unique chlorine-perovskite interlayer which enhanced charge extraction by bonding with the SnO_2 ETL layer. This resulted in a record efficiency of 25.8%. [30]

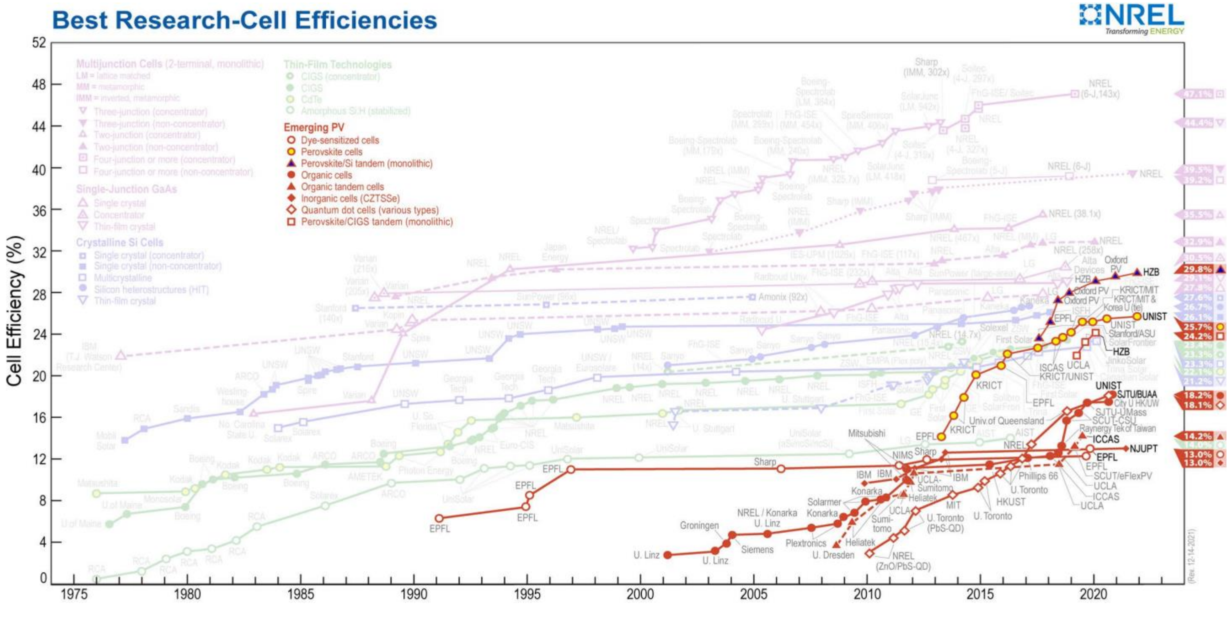

Figure 7. Plot of Best Research-Cell Efficiencies, Emerging PV. This plot is courtesy of the National Renewable Energy Laboratory, Golden, CO. [31]

2.2.4 Research Trends

2.2.4.1 Scalability

One of the most notable research trends in the field is the push to explore scalable fabrication techniques. To deposit the perovskite layer, the precursors are dissolved into solvents to create a perovskite ink. There are a variety of methods to deposit this ink, some more scalable than others. Scalable processing is any process that can meet the high throughput requirements of large-scale operations. This typically implies fast deposition, minimal waste, and the ability to be deposited in ambient conditions. A common scalable process is called roll-to-roll processing (R2R), which is a continuous process in which rolls of flexible substrates pass under and through machines that deposit and crystallize perovskite films. Because roll-to-roll is highly efficient, a significant amount of research is currently focused on producing PSCs in this fashion.

Spin coating has been the dominant method of perovskite deposition due to its simplicity, consistency, and low cost. Spin coating is performed by dropping perovskite precursor ink onto a substrate and then spinning it for a designated amount of time at a specific rate of rotation. The centrifugal force generated by this motion pushes the ink outward from the center and creates a thin film. The thickness can be easily controlled by the spinning rate and concentration of precursor ink. Unfortunately, spin coating is not a practical deposition method for large-scale production of PSCs. Not only does spin coating limit devices to small areas, but it's also extremely wasteful. Most of the ink that is dropped onto the substrate is spun off within the first few seconds of coating. To address this problem, alternative perovskite deposition methods have been explored.

In recent years, many PSC studies have centered around the idea of scalable processing. Some of the popular proposed methods include slot-die casting, blade coating, and inkjet printing. Slot-die casting is the process of pushing ink through a slot die head, which deposits a thin strip of ink uniformly across a substrate. The thickness can be controlled by adjusting the speed at which the substrate moves under the slot die head, as well as the ink deposition rate. The rheology of an ink also plays a role in film thickness and formation. There are a few demonstrations of this technique giving rise to high-performing PSCs. [32][33] Most notably, J. Li et al. used a slot-die casting followed by passing the deposited film under a nitrogen gas air knife to achieve a PCE of 20.8% [34]

Blade or bar coating is a similar process, which simply pushes already deposited ink under a doctor blade, or bar, to smooth out the surface. The gap between the substrate and the blade influences the final film thickness. Blade coating is less common than slot die casting, but there have been promising results so far. Recently, C. Li et al achieved a PCE of 18.2% using zinc porphyrin additives to control crystallization and passivate defects. [35] Unfortunately, slot-die casting and blade coating are limited in the final shape that they can deposit. Unless a mask is used, and ink is wasted, only rectangular areas can be achieved.

Inkjet printing is another scalable method for perovskite deposition and will be the focus of this project. In this method, ink is ejected from a printhead directly onto the substrate, making for cost-effective and material-efficient deposition. The primary advantage of inkjet printing over the previously mentioned techniques is in its ability to deposit precursor solution only where it is needed, as well as deposit active areas in a larger variety of shapes. There have been several successful PCSs fabricated with the help of inkjet printing. P. Li et al. used inkjet printing to print PbI_2, followed by exposure of the film to MAI vapor, to achieve a large area (2.02 cm^2) PCE of 17.74%. [36]. Regarding one-step inkjet printed PSCs, many successful attempts have been made as well. H. Eggers et al. developed a triple cation ink that initially recorded an efficiency of over 21% (stabilized PCE of 18.5%). [5] Z. Li et al. developed a triple cation-based ink which resulted in PCEs of 19.6% and 17.9%, for 0.04 and 1.01 cm areas, respectively. [2] C. Liang et al. created $MAPbI_3$ based PSCs with small (0.04 cm^2) and large (4.0 cm^2) area PCEs of 17.04% and 13.27%, respectively, using a vacuum-annealing treatment. [3] L. Zhang et al. achieved a stabilized PCE of 16.6% by printing $MAPbI_xCl_{3-x}$ film in ambient conditions. [37] The natural evolution in the field of inkjet printing is a fully inkjet printed device. In 2021, F. Schackmar et al. developed an all-inkjet printed PSC (apart from the ITO and Au electrodes), with a PCE of just over 17%. [4]

The advantages of inkjet printing have also recently been used in industry. A Polish manufacturer of perovskite solar technology, Saule Technologies, has been using inkjet printing to process innovative perovskite solar cell-based technology, such as solar sun blinds and photovoltaic window glass. [38] Building-integrated photovoltaics such as these often require unique strict control over that area of deposition, which cannot be practically achieved using slot die casting or bar coating. The working mechanisms behind inkjet printing will be discussed in section 2.3.

Solvent removal is an equally crucial component of the perovskite deposition step and must also be adapted for scalable processes. This topic will be discussed further in section 2.4.3.

2.2.4.2 Stability

Another trend in the field of perovskite solar cells is the push to increase the stability of perovskites so that they can compete with the standard 20-year operating lifetime that is standard in most silicon panels. Perovskite, particularly $MAPbI_3$, is inherently unstable. This is partly due to the weak van der Waals interactions that hold the organic and inorganic components of $MAPbI_3$ perovskite together. [39] Furthermore, perovskites are susceptible to ion migration, which accelerates degradation, and can be induced by moisture, light, or heat exposure. [40][41] Ion migration can increase defect density and thus recombination, which can build over time. [39][40] H_2O has additionally been shown to degrade perovskite films, as it forms complex hydrate products. [40] O_2 has also been shown to attack the methylammonium ion in the $CH_3NH_3PbI_3$ structure, forming unwanted products. [39]

There are two general approaches to addressing these issues. The first is a chemistry-based approach that explores new perovskite chemical analogs for enhanced stability and defect tolerance. This has been the most common approach in the field of PSCs. Typically, the methylammonium A site in the ABX_3 perovskite formula is partially substituted with formamidinium (FA) and/or cesium (Cs). Simultaneously, PbI_2 can be partially substituted with other lead salts such as $PbBr_2$. There are several suggested mechanisms in which multiple cation-based perovskites deliver enhanced stability. FA is a larger cation than MA, which naturally gives the FA-based perovskite a higher tolerance factor. Alloying FA with Cs allows for tolerance factor tuning, which determines the likelihood and stability of favorable and unfavorable perovskite phases. [42] M.J. Hong et al. reported that, unlike $MAPbI_3$, $FAPbI_3$ charge carrier mobility is not as affected by the hydrate products that are formed, as devices are inevitably exposed to moisture over time. [43]

A second approach for enhancing the stability of perovskite films is through the addition of polymer additives directly into the film. Recently, there have been many studies documenting the ability of polymer additives to enhance the stability and PCE of perovskite solar cells. This method of introducing polymers into the film will be discussed in section 2.5, as it is the approach that will be taken in this work.

2.2.5 Application of Perovskite Solar Cells

As a thin-film solar cell, PSCs have many advantages over traditional c-Si cells. Perovskite modules could go in places where bulky c-Si panels would not fit. PSCs have been successfully processed on flexible substrates, which could open doors for applications such as wearable electronics, avionics, and space missions. [44] [45] PSCs are also lightweight, which is a useful attribute in almost any application. The semi-transparency of PSCs can be useful for the discrete collection of light on structures such as windows and roofs. The ability to tune perovskite’s bandgap has made it a great candidate for tandem solar cells. Silicon-perovskite solar cells have shown great potential for applications where high current density is needed. [46][47]

2.3 Inkjet Printing

Inkjet printing (IJP) is the most practical way to deposit thin films onto a substrate, but in many ways, it is the most complicated. The first work on inkjet printing was carried out in the 1940s by C.W. Hansell. It was not until 1977 that the first inkjet printer became commercially available. [48] In the past few decades, inkjet printing has evolved into an extremely precise and cost-effective approach for the deposition of ink, whether it be printer ink on paper, or conductive precursor solution onto a substrate. It was not until 2014 that inkjet printing was utilized in the deposition of perovskite precursor ink for solar cells. [49] Since then, inkjet printing has been developed into an extremely viable method of perovskite deposition. This section will introduce the basic working mechanisms behind this technology and discuss the parameters in which inkjet printing can operate.

2.3.1 Working Principles of Inkjet Printing

Inkjet printing is a process in which droplets of ink are jetted out of a printhead and onto a substrate. The printhead assembly is made up of an ink reservoir, a dispensing element, and a printhead tip, as seen in Fig. 8. The dispensing element contains a piezoelectric transducer which creates pulses that apply forces onto the ink, causing it to expand and compress, which generates droplets. The waveform must generate forces with enough magnitude to overcome the cohesive forces in the ink and the adhesive forces between the ink and printhead. Viscous or high surface tension inks tend to require greater force, and thus higher voltage, for ejection from the printhead. If too much force is applied, the ink may not stay together in one cohesive droplet. Droplet volume tends to be on the scale of tens of picolitres and is dependent on the printhead orifice. Printhead orifices tend to be anywhere from 10-100 microns in diameter.

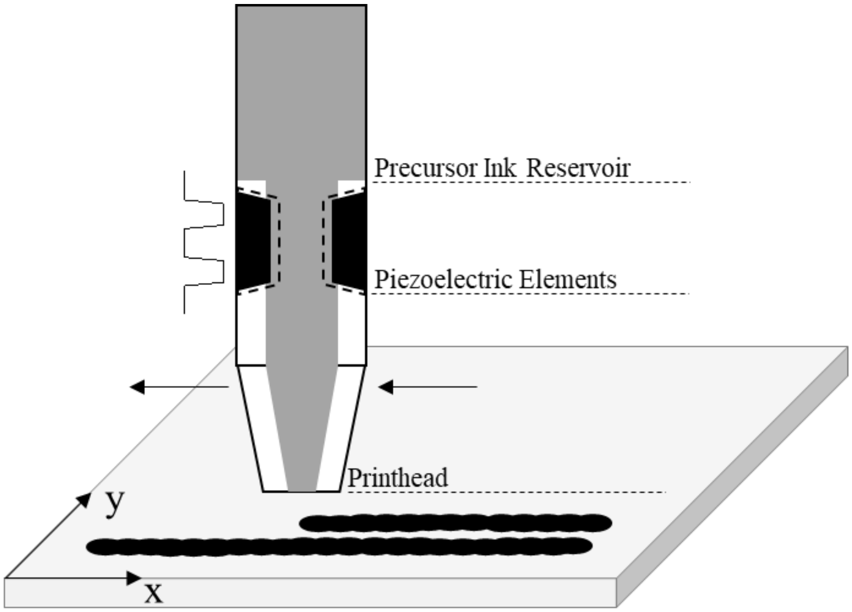

Figure 8. Schematic of an Inkjet Printhead.

The printability of an ink is described by the Ohnesorge number (Oh), which is a dimensionless parameter that describes the likelihood of a droplet maintaining its shape upon ejection from the printhead. The Oh number is defined in Eq. 4.

$$Oh = \frac{\eta}{\sqrt{\rho \cdot \sigma \cdot d}} \tag{2-4}$$

In Eq. 4, η is dynamic viscosity, ρ is density, σ is surface tension, and d is the diameter of the printhead orifice.

As seen in Fig. 9a, the generation of stable droplets requires an Oh between 0.1 and 10. [50] This range represents a balance of viscous dissipation and internal surface tension forces that will be sufficient to generate droplets that stay together upon ejection. If the Ohnesorge number is too low, which commonly results from inks that are not vicious enough, satellite droplets may be generated. Satellite droplet formation can be seen in Fig. 9c. In this case, the droplets' internal cohesive forces are not large enough to overcome the applied forces from the piezoelectric pulse, and the trailing ligament will be separated from the primary droplet. It is important to keep drop size consistent from batch to batch since inconsistent droplet size will change the amount of deposited ink. Satellite droplets make it hard to determine exactly how much ink volume is ejected and can also deviate from the direct path between the printhead and substrate, decreasing the resolution of the pattern. If an ink's Ohnesorge number is too high, the system may struggle to produce droplets, as most of the applied forces are dissipated by the ink's high viscosity. Furthermore, overly viscous inks tend to not form uniform films, as some degree of ink spreading on the substrate is necessary to create a continuous film. The inks Reynolds number, which is dependent on the ink's velocity, also determines a solution's printability and behavior on the substrate. The higher the Reynolds number, the more likely the ink will splash as it makes contact with the substrate, which is not conducive to uniform film formation.

The waveform, as seen in Fig. 9b, controls the magnitude and duration of the pulses. A balance between applied voltage, rise time, dwell time, and fall time must be optimized for each ink. Pulses tend to last no more than 30 μs, and the voltage usually does not exceed 50 V for inks in the acceptable printing range.

2.3.2 Inkjet Printing Perovskite

To inkjet print perovskite, a precursor solution must be made. This is done by dissolving precursor solutes into solvents until the ink achieves a viscosity, density, and surface tension that is suitable for droplet formation, as dictated by the Ohnesorge number. Before the ink is loaded into the reservoir, it is usually filtered through a filter with a pore size several magnitudes smaller in size than the diameter of the printhead. This will mitigate the chances of clogging the printhead. Larger orifices, and thus larger droplets, struggle to create sharp, high-resolution patterns and edges. Smaller orifices offer higher resolution but run a higher risk of clogging.

Single nozzle systems are not practical for large-area devices. Due to the limited deposition capabilities of a single nozzle, these setups require longer processing times that are not ideal for perovskite thin films, as excessive solvent evaporation and long environmental exposure before annealing can lower the film quality. Multiple printhead systems are generally more suitable for depositing large active areas. Depending on the system, either the printhead assembly or the stage below, will be in motion. The motion is dictated by a script, in which the operator specifies a variety of parameters including starting position, drop spacing, print pattern, and print speed.

Perovskite precursor ink can be applied in a one or two-step fashion. In one-step printing, the precursor ink contains all the necessary solutes to convert into crystalline perovskite. Two-step printing involves the back-to-back deposition of separate perovskite components, which may offer more control over the crystallization of the film [36]. This work will explore the potential of one-step printing, as to make the system as simple and scalable as possible.

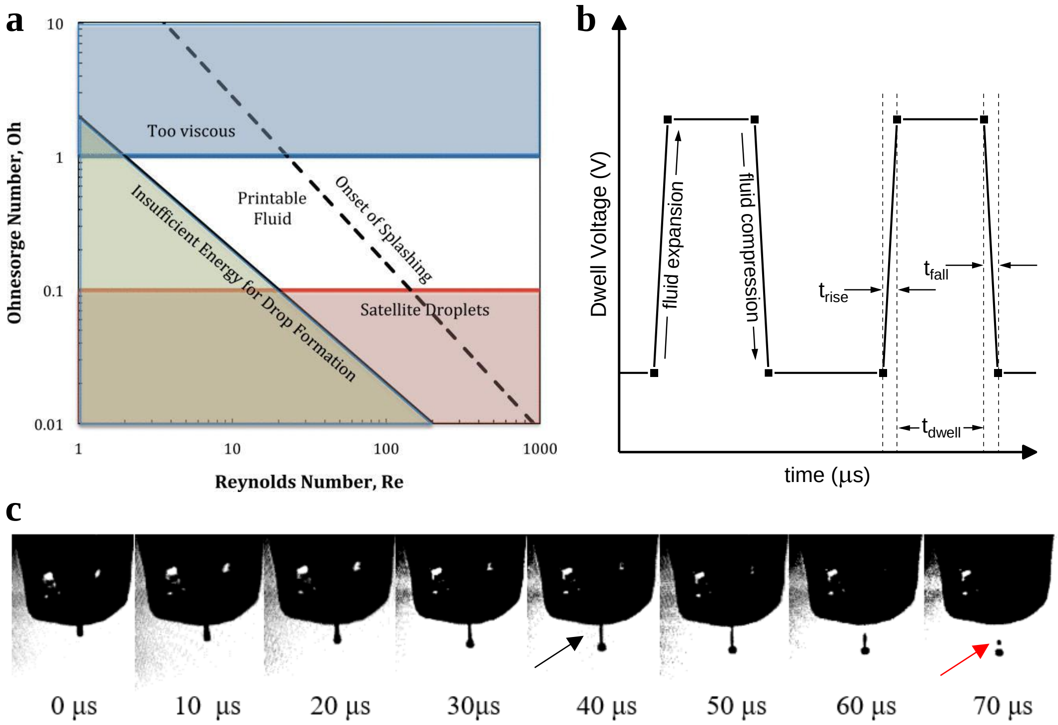

Figure 9. Inkjet Droplet Formation. (a) Ohnesorge vs. Reynolds number, graph reproduced with permission from [50]. (b) Piezoelectric waveform parameters. (c) Formation of satellite droplet (red arrow). The black arrow is the ligament.

2.4 Solvent Engineering

Solvent Engineering is the process of optimizing the solvents used for the precursor solution, as well as the antisolvents used for solvent removal and generation of the intermediate phase, which is important for dense and uniform films. This section will cover the role of solvents in the film, the generation of the intermediate phase, and the practicality of common solvent removal methods.

2.4.1 Role of Solvents

The primary role of solvents in precursor solution is to dissolve the solute precursor components so that a solution can be optimized for deposition. Common solvents are dimethyl sulfoxide (DMSO), dimethylformamide (DMF), γ-butyrolactone (GBL), and n-methyl-2-pyrrolidone (NMP). These solvents have good solubility with MAI and PbI_2. The concentration of solvents to solute, as well as properties such as vapor pressure, boiling temperature, viscosity, and affinity to precursor components, must be considered when creating a solvent system, as these parameters directly correlate to film formation.

A binary solvent system is typically used to dissolve the perovskite precursor components. DMSO is commonly paired with a secondary solvent, such as DMF, because of its chemical affinity to the PbI_2. DMSO is a Lewis base and can donate its non-bonding electrons of oxygen to form an adduct with the Pb^{2+} in PbI_2, which can be considered a Lewis acid. [51][52][53][54] MAI can also be considered a Lewis base because MAI can donate electrons of its iodide ion (I^-). [51][52] It is the DMSO-PbI_2 relationship that is the primary driving force for intermediate phase generation. The secondary solvent's main purpose is to tune the concentration and rheology of the precursor solution.

2.4.2 Generation of the Intermediate Phase

Due to the strong attraction between DMSO and PbI_2, an intermediate phase, commonly expressed as $MAI{\cdot}PbI_2{\cdot}DMSO$, can be formed. Some reports specifically identify this phase as $MA_2Pb_3I_8{\cdot}2DMSO$. [55][54] The intermediate phase is induced when the film becomes saturated due to the rapid removal of the secondary solvent. The highly saturated film triggers the intercalation of MAI and DMSO into the layered structure of PbI_2, which is held together by weak van der Waals bonds. [53][55] This leads to an expansion in the c-axis of the crystal structure. It is generally accepted that the use of DMSO and thus the formation of the intermediate phase is beneficial for the formation of dense perovskite films. [56][51] DMSO retards the interaction between MAI and PbI_2, which preserves the film and delays conversion into perovskite until the annealing step. In films with no DMSO, the excessively facile formation of perovskite at the antisolvent-perovskite interface would induce grain growth from the top, which leads to small grains and poor interfacial contact with the bottom electron conduction layers. [51]

2.4.3 Nucleation and Crystallization of Perovskite Films

The final morphology of the film is largely dependent on the generation rate of nucleation sites, as well as the rate at which perovskite grains grow. These parameters are determined by the concentration of the solution. If the evaporation or removal of solvents from a solution is slow, then the film will spend most of its time before annealing at a concentration that is too low for nucleation to begin, but high enough for rapid grain growth. As a result, large crystals grow upon thermal annealing from a small number of nucleation sites, forming a discontinuous film. [57][58][59] In this case, the discontinuities in the film would lower the shunt resistance to a point where almost no voltage can be accumulated. Alternatively, if solvent removal is achieved quickly, which provides the high concentration environment that is needed for nucleation, many grains will grow and form a dense, compact film. [57][58][59]

The use of antisolvents has been the most common way to rapidly wash away the secondary solvent and induce the intermediate phase. Antisolvents are solvents that are not soluble with the solute but are miscible with the solvents of the solution. When a solution is exposed to an antisolvent, the secondary solvent rapidly diffuses out of the film until the solutes MAI and PbI_2 become supersaturated, allowing for intermediate phase formation. Unless the DMSO has formed coordination bonds with the perovskites, it too will be washed away. [53] After antisolvent treatment, the precursor solution is effectively frozen in place due to the absence of solvent. The intermediate phase forms very rapidly. After the $MAI \cdot PbI_2 \cdot DMSO$ phase is formed, nucleation may commence if the film is continuously exposed to antisolvent.

Antisolvent solvent removal is usually associated with antisolvent dripping, a method in which an antisolvent is dropped onto a perovskite film partly through the spin coating step. This method is only applicable for spin-coated films and is thus not an option for other scalable deposition methods. The method has however been used in most of the record PCE devices to date, including the previously mentioned study by H. Min et al. [30] Research in the field has aimed to explore scalable methods of solvent removal that are compatible with scalable deposition.

As previously mentioned in section 1.0, there have been numerous successful reports of using a vacuum to induce rapid solvent evaporation and eventual perovskite intermediate phase, most of which rely on inkjet printing for precursor deposition. [1]–[5] Vacuum flashing is usually done by placing individual cells in a vacuum chamber, followed by thermal annealing. One of the most notable vacuum flash studies came from H. Eggers et al., who used inkjet printing and vacuum flashing to induce nucleation of micrometer-thick films, resulting in a PCE of over 18%.[5] While this process negates the use of an antisolvent, it is not compatible with continuous or high-throughput processing.

Antisolvent bathing is a scalable solvent extraction method that has been sparsely developed for the application of perovskite solar cells. In this method, the deposited film is submerged or rolled into a reservoir containing antisolvent. Upon submersion, diffusion of the precursor solution's solvents occurs almost instantaneously. Due to the continued exposure to antisolvent, nucleation can begin after intermediate phase formation, which is usually marked by a change in color, as seen in Fig. 10. The bathing time is dependent on how fast the antisolvents can remove the solvents and the degree of nucleation that is desired before thermal treatment. This method of solvent extraction, unlike vacuum flashing or antisolvent dripping, is scalable.

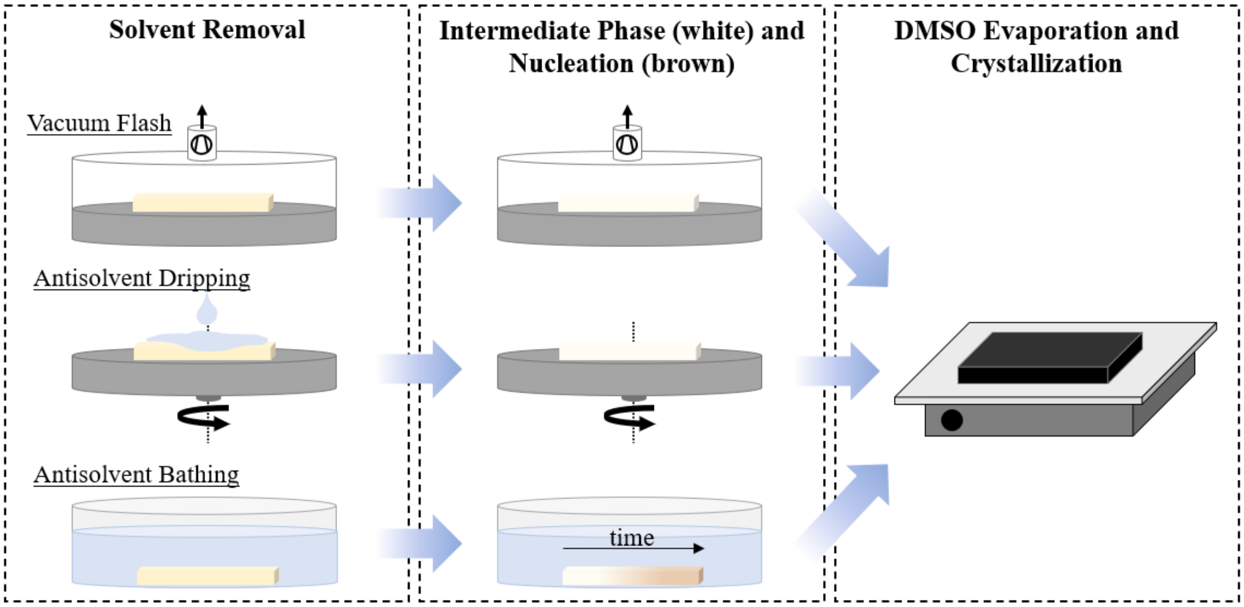

Figure 10. Common Solvent Removal and Intermediate Phase Formation Methods.

There have been a few promising reports of dense films made using antisolvent bathing. For example, Y.Y. Kim et al. gravure-printed perovskite onto flexible substrates, followed by antisolvent bathing, to achieve a PCE of 16.7% [7] Another interesting finding came from G. Jang et al. They found that if the antisolvent bath temperature is cooled down, the rate of nucleation will slow, giving rise to large grains. Using this cold antisolvent method, they achieved champion devices with a PCE of 18.5%. [60]. Vacuum flashing, antisolvent dripping, and antisolvent bathing are visualized in Fig. 10.

Another promising and scalable method of solvent extraction is called hot casting. Hot casting is defined as the deposition of a precursor ink directly onto a hot substrate, negating the need for an antisolvent. Some studies claim that the intermediate phase is never induced, citing the accelerated diffusion and interaction between solutes was sufficient for large, densely-packed grains to form. [61][62] The transformation from the liquid phase to the perovskite phase only takes a few seconds, so the intermediate phase, which preserves the film, is not necessary.

Annealing is the last step in the process. It is only during this step that the coordinating DMSO is evaporated, allowing for the conversion from the intermediate phase to perovskite. Annealing conditions depend on the perovskite analog. The common $MAPbI_3$ films are usually annealed in the range of 95-110°C, while formamidium-based perovskites require temperatures closer to 150°C.

2.5 Polymer-Composite Films

A perovskite-polymer composite film is made by dissolving small amounts of polymer into the precursor solution. The polymer chains stay in the film after crystallization, occupying grain boundaries. The enhanced performance and stability of composite devices that are often reported can be attributed to many mechanisms relating to crystal growth kinetics and final microstructure. Commonly investigated polymers include polyvinylpyrrolidone (PVP), polypropylene carbonate (PPC), and polymethyl methacrylate (PMMA), which are all Lewis bases.

Polymers tend to have a grain-to-grain cross-linking effect in polycrystalline films, meaning that grains are effectively connected via polymer networks. [13] As such, cross-linked polycrystalline films can exhibit reduced electrical decoupling, enhanced stability, and longer carrier lifetime, which are attributes usually associated with monocrystalline films. [13] The driving force for cross-linking are the bonds between the polymer, which commonly behave as Lewis bases, and the dangling Pb^{2+} ions found at the grain boundaries. [10][11][63] These grain boundary passivation effects can also reduce non-radiative recombination, which releases unwanted vibrational phonons. This is due to the slowed crystallization kinetics and thus suppressed the formation of defects such as vacancies or anti-sites in the perovskite structure. [10][8] Increased surface coverage is also be explained by polymers occupying the gaps between grains. [9][11] Dense films are desired, as the lack of pinholes and discontinuities in these films mitigates current leakage, which increases shunt resistance. Thin polymer coatings have also been explored. The high bandgap of polymers can act as an effective electron barrier between the active layer and hole transport layer, which can reduce recombination and increase voltage. [64]

Stability has been shown to dramatically increase in devices made with polymer-perovskite composites. The slower degradation is attributed to the same grain boundary passivation effects that enhance the performance of the devices. Grain boundaries act as recombination hot spots, lower overall carrier mobility through the device, and act as avenues for ions or impurities to travel through. [13] The dangling bonds that exist in grain boundaries often form bonds with impurities such as oxygen and water, which create complex adducts and hydrate products that can break down the film over time. [39] Reduced ion migration [11][8], and overall enhanced rigidity that polymers induce are beneficial to the longevity of the perovskite film. There are conflicting reports regarding the effect of polymers on grain size, which may suggest that the rate of grain growth, or density of nucleation sites, is affected by the type of polymer. Some reports have found that polymer addition increased grain size, which could be explained by an increased nucleation activation energy, which lowers the density of nucleation sites, giving rise to large grains. [13] Contradicting reports have found polymers to decrease the grain size. [63][12] In these cases, an argument could be that the slowed crystallization may have given more time for nucleation site formation. It should be noted that in both scenarios, the stability and efficiency were still enhanced, meaning that any damaging effects arising from small grain size were compensated by the positive effects of inter-grain passivation.

2.6 Analysis and Characterization of Perovskite Solar Cells

Scanning electron microscopy (SEM) is an invaluable tool for the analysis of thin-film quality. Overhead, or top-down images reveal grain size and film discontinuities such as pinholes. The grain size was calculated using the intercept method, where lines of known length are drawn across an SEM-obtained image, and the number of grain boundaries that intersect the line are summed. The average grain size can be determined by dividing the length of the line by the number of intersections. For grain size calculations, at least 3 lines of even spacing are drawn over each picture and then averaged for an accurate depiction of grain size. Cross-sectional SEM images were obtained for examination of the interfaces between each layer, as well as the thickness of each layer.

X-ray Diffraction (XRD) is the primary characterization technique used in this work. XRD can identify crystal structure, which can be used to characterize films. The Bragg law is useful in the characterization of crystalline materials, as it relates the detected diffraction angle with the interatomic spacing of a crystal lattice. The Bragg law is given below in Eq. 5.

$$n \cdot \lambda = 2 \cdot \mathrm{d} \cdot \sin\theta \tag{2-5}$$

In the Bragg law, n is the order of diffraction, λ is the incident wavelength, d interatomic spacing, and θ is the diffraction angle. $MAPbI_3$ perovskite has many recognizable diffraction peaks, most notably the (110) and (220) plane peaks located at the 2θ diffraction angles of about 14.1° and 28.2°, respectively. The PbI_2's 12.6° 2θ diffraction angle is often used to identify the degree to which the perovskite is formed. The presence of this peak initially implies incomplete conversion of PbI_2 into perovskite.

The intensity of the PbI_2 peak relative to the perovskite peaks can also be used to characterize the degree of degradation, as perovskite collapses into its precursor components over time. Peak intensity is an indication of the degree of crystallinity or long-range order. Deficits in peak intensity can indicate the presence of impurities or poor crystal formation. XRD can also be used to analyze the concentration of internal stresses and the amount of strain in the crystal structure. Although there are many factors that can affect the shape and location of the peak, grain size and internal strains are most cited as causes for peak broadening and shifting in polycrystalline films. Internal stresses, which can be brought on by grain boundaries, cause strain in the crystal lattice. This induces peak broadening. [65] More specifically, broadening is generally caused by non-uniformly distributed strain, which slightly changes the interplanar spacing and thus the diffraction angle. The combination of many slightly different diffraction angles causes the peak to have a broader shape. If internal strains are uniformly distributed peak, shifting will occur. The shift direction depends on if the stress is compressive (smaller interplanar spacing) or tensile (larger interplanar spacing), and it is thus useful to understand the correlation between diffraction angle and interplanar spacing, given by Bragg's law.

The degree of XRD broadening can be used to estimate grain size as well, using the Scherrer equation, found in Eq. 6.

$$t = \frac{K\lambda}{\beta \cdot \cos\theta_B} \tag{2-6}$$

In the Scherrer equation, t is the mean grain size, K is a dimensionless shape constant usually accepted as 0.9, β represents the degree of peak broadening at half the maximum intensity, and θ_B is the diffraction angle. This equation only describes the relationship between peak broadness and grain size and should not be used to strictly declare the grain size of a material. It cannot account for factors such as instrumental effects, and many only consider it suitable for grains under 100 to 50 nanometers. [66] XRD can also be used to determine other crystalline layers in the stacked device, such as TiO_2 and FTO. This can be useful for determining the degree of surface coverage, or grain density, in the film. X-rays have a penetration depth much shorter than the thickness of most perovskite films, so peaks of material underneath the perovskite indicate there are discontinuities or pinholes in the film for the X-rays to travel through. Amorphous materials such as glass substrates do not produce well-defined peaks.

Many other analysis and characterization techniques were used to obtain data for this project. Fourier transform infrared spectroscopy (FTIR) was used for the analysis of perovskite-polymer films, as FTIR characteristic peaks were able to detect chemical interactions between polymers and perovskite. A rheometer and drop shape analyzer were used to determine the viscosity and surface tension of precursor solutions, respectively, which was valuable information in determining the printability of the inks. Optical microscopy was used to analyze the spreading behavior of the precursor ink on the substrate. Solar simulators and IPCE instrumentation were necessary for assessing the quality of the PSCs.

3.0 Research Description

3.1 Hypothesis

To address the scalability and stability of perovskite-polymer solar cells, the functionality of a novel inkjet printing to antisolvent bathing system in an ambient processing environment will be tested. The hypothesis has 3 parts: 1) Several parameters relating to ink rheology and substrate preparation will affect the printability and spreading of the precursor ink, which will influence the final film morphology. 2) Antisolvent bathing can rapidly wash solvents from the film, inducing the intermediate phase, and eventually leading the formation of dense polycrystalline films. 3) Polymer additives can form Lewis-base adducts with the perovskite, where it can occupy grain boundaries. This may enhance device stability and reduce electron-hole recombination, which could increase current density and power conversion efficiency.

3.2 Project Objectives

The objective of this work is to explore the relationships among inkjet printing parameters, solvent systems, antisolvent conditions, and film formation. Regarding stability, many polymer concentrations in perovskite ink must be tested to explore the full potential of this approach. We want to rely on a wide variety of analysis and characterization techniques to propose mechanisms regarding film formation and polymer-induced grain boundary passivation. This data should be a useful reference for future inkjet printing and perovskite-polymer studies.

4.0 Experimental

4.1 Materials

All chemicals, unless otherwise stated, were purchased from Sigma-Aldrich. Chemical synthesis is carried out in a nitrogen glove box. The deposition process for each device layer, unless otherwise stated, is carried out in ambient conditions, under a fume hood.

Blocking layer TiO_2 is prepared by mixing titanium diisopropoxide bis(acetylacetonate) (75 wt.% in isopropanol) and 1-Butanol (TCI Chemicals, >99 %) in a volumetric ratio of 0.971:4. The solution is mixed with a stir bar for 1 hour at room temperature and before storing at 5°C for at least 2 hours before deposition. Mesoporous TiO_2 is separately prepared by dissolving TiO_2 paste (Interpero) in ethanol (Decon Labs, 200 proof) in varying volumetric ratios. The solution is placed in an ultrasonic cleaner to disperse TiO_2 particles.

Perovskite solution is prepared by dissolving a 1:1 molar ratio of MAI (Oscilla, >99.9 %) and PbI_2 (99%) in various ratios of DMF (99.8 %) and DMSO (>99.9 %). The solution is stirred at room temperature for 3 hours with a stir bar.

The Spiro-OMeTAD solution is prepared by mixing 36 mg of 2′,7,7′-tetrakis-(N,N-di-p-methoxyphenylamino)9,9′-spirobifluorene (Lumtec, 99.8%) in 500 μL chlorobenzene (99.8%) and 14.4 μL of 4-tert-butylpyridine (96%), while separately mixing 360 mg of (bis(trifluoromethane) sulfonimide) (99.95%) in 500 μL of acetonitrile (99.8%). These two solutions are mixed with a stir bar separately for 15 minutes, before 8.8 μL of the (bis(trifluoromethane) sulfonimide) solution is added to the spiro-OMeTAD solution. This final solution is stirred at room temperature for an additional 15 minutes before deposition.

4.2 Device Fabrication

FTO glass substrates (Pilkington, TEC8) are cut into 2x2 cm squares. Substrates are masked with tape and etched using zinc powder (Alfa Aesar, 97 %) and a solution of 1:1 hydrochloric acid:deionized water to remove a strip of FTO on the anode side of the device. After etching, samples are cut, numbered, and cleaned in an ultrasonic cleaner with three consecutive baths of acetone, deionized water, and ethanol, in that order. Samples are blown dry with compressed air, before further cleaning in a Jaesung Engineering UVC-30 UV-Ozone cleaner.

For TiO_2 deposition, samples are first masked with tape on the cathode side of the device (opposite of etched side). Blocking layer TiO_2 is deposited by dropping 50 μL of the solution onto a substrate, spinning at 3000 rpm for 30 seconds, and finally placing on a hotplate set to 150°C for 15 minutes. Next, the samples are spin-coated with mesoporous TiO_2 by dropping 50 μL of the solution onto the substrate and spinning at 4000 rpm for 30 seconds, followed by heating at 60°C for 90 seconds to evaporate ethanol. The spin coater used is a Laurell Technologies WS-400BZ-6NPP/LITE. Mesoporous TiO_2 is scraped off the cathode side, and substrates are annealed at 500°C for 90 minutes in a furnace. Before inkjet printing, TiO_2-coated substrates are cleaned in the same UV-Ozone generator for 15 minutes.

The inkjet printer used was a MicroFab Technologies JetLab 4 with the PH-41 printhead assembly and 60 μm printhead orifice. The precursor ink was filtered through a PTFE 0.45 μm filter to reduce the likelihood of clogging. The waveform voltage parameters are dependent on the precursor ink, but the rise times, dwell/echo times, frequency, and back pressure remained constant at 4 μs, 25 μs, 1000 Hz, and -3.8 psi, respectively. The dwell voltage varied from 30-33 V. The droplet spacing primarily used was 0.12 mm in the x-direction and 0.20 mm in the y-direction.

After printing, films were immediately transferred into an antisolvent bath for anywhere from 3-15 seconds. Substrates are moved with tweezers to ensure even application of antisolvent across the film. Next, the samples are transferred to a hotplate to crystallize at 100°C for 10 minutes.

Spiro-OMeTAD was deposited by dropping 35 μL of solution and spinning at 4000 rpm for 30 seconds. Unwanted Spiro-OMeTAD is then scraped and wiped away from the cathode side. Finally, devices are inserted into a custom shadow mask for the application of gold electrodes using a Plassys 8 Pocket E-Gun Evaporator. The system is run at a deposition rate of 0.05 nm/s until a thickness of 70 nm is achieved.

4.3 Analysis and Characterization

X-ray diffraction was performed on a Bruker D8 Discover SRD diffractometer. The target used was standard Cu-Kα radiation with a wavelength of 1.5406 Å. Measurements were taken from 10° to 60° (2θ). A step size of 0.02° and a step interval time of 0.5 seconds were chosen for measurements.

Scanning electron microscope pictures were obtained using a ZEISS Sigma500 VP electron microscope. To reduce the charging of the glass substrate, samples were masked and mounted with conductive tape and silver paste. Scans were taken at a voltage of 2-3 kV and used an in-lens detector. A top-down, or overhead view was utilized for grain size determination and film continuity analysis, and cross-sectional images were used for thickness determination and interfacial contact analysis.

Fourier transform infrared spectroscopy measurements were taken on a Bruker Vertex-70LS FTIR system, using the attenuated total reflection method. Measurements were taken from 4000 to 500 cm^{-1}. Polymer-perovskite samples were deposited on infrared-transparent silicon wafers, as opposed to typical FTO glass-based substrates. An uncoated silicon wafer was used as a reference to filter out peaks that were not of interest. Baseline correction and Savitzky-Golay smoothing (50 points of window) were performed to make data comparable and free from noise.

Optical microscopy for ink spreading and drop spacing pictures were obtained from a Zeiss Smartzoom 5 microscope. Samples were printed on top of glass/FTO/bl-TiO_2/m-TiO_2 substrates to mimic the actual spreading behavior of ink on devices intended for complete solar cell fabrication.

IV curves were obtained using a solar simulator (PV Measurements Inc.) which simulated AM1.5G using an input power of 100 mW·cm^2. Forward bias scans were run from 1.2 to -0.1 V for reverse scans, and -0.1 to 1.2 V for forward scans. The scan rate was run at 0.1 V/s, with a sensitivity of 0.001 A/V.

For IPCE measurements, a monochromator, light source, illuminator, and Si reference cell were all from Newport. Measurements were taken from 200 to 900 nm with a step size of 10 nm.

5.0 Results

5.1 Schematic of Perovskite Solar Cell

A schematic and SEM cross-sectional image for the design of the inkjet printed PSC can be found in Fig. 11. The device architecture is identified as mesoporous n-i-p, as light comes through the glass/FTO/TiO_2 side. The perovskite chosen was $MAPbI_3$, and was the only inkjet printed layer. The ETL material was mesoporous-TiO_2 (m-TiO_2) deposited on top of compact TiO_2. The HTL transport layer was Spiro-OMeTAD. The transport layers were spin coated, and the gold electrodes were evaporated using physical vapor deposition, as detailed in section 4.2. The processing was done in an ambient environment, apart from the physical vapor deposition for the application of the electrodes.

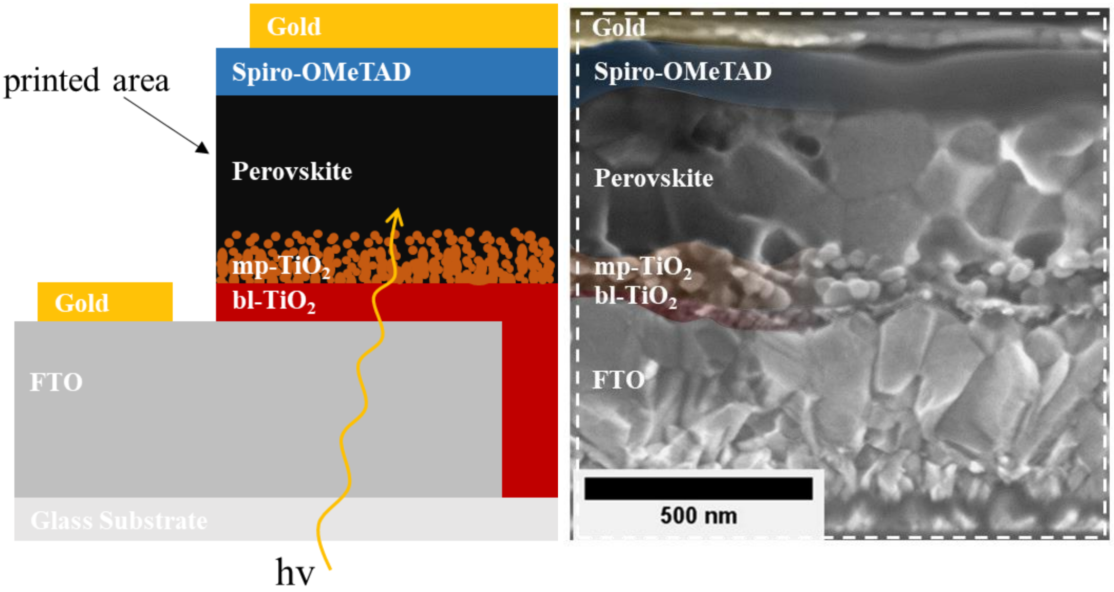

Figure 11. Mesoporous n-i-p perovskite solar cell architecture. (a) cross-section schematic of n-i-p PSC (b) Scanning electron microscope cross-section image of n-i-p PSC.

5.2 Inkjet Printing Perovskite Films

The process, from perovskite deposition to crystallization, is visualized in Fig. 12. Processing time between steps was minimized by keeping the printer, antisolvent bath, and hot plate nearby each other. Substrates were put into the inkjet printer one at a time. After printing was completed, devices were swiftly moved to the antisolvent bath. The intermediate phase could be identified by the almost instantaneous color change from bright yellow to translucent white. Nucleation was identified by a further color change from light to dark brown. Finally, the substrate was moved to the hot plate for thermal annealing. This process was repeated for each batch, which usually consisted of around 20 samples. The antisolvent bath was never replenished for a batch, and all steps were carried out in ambient conditions.

This section will cover the optimization of printing parameters, ink rheology, and substrate preparation, as well as explore how each parameter affects the formation of the thin film.

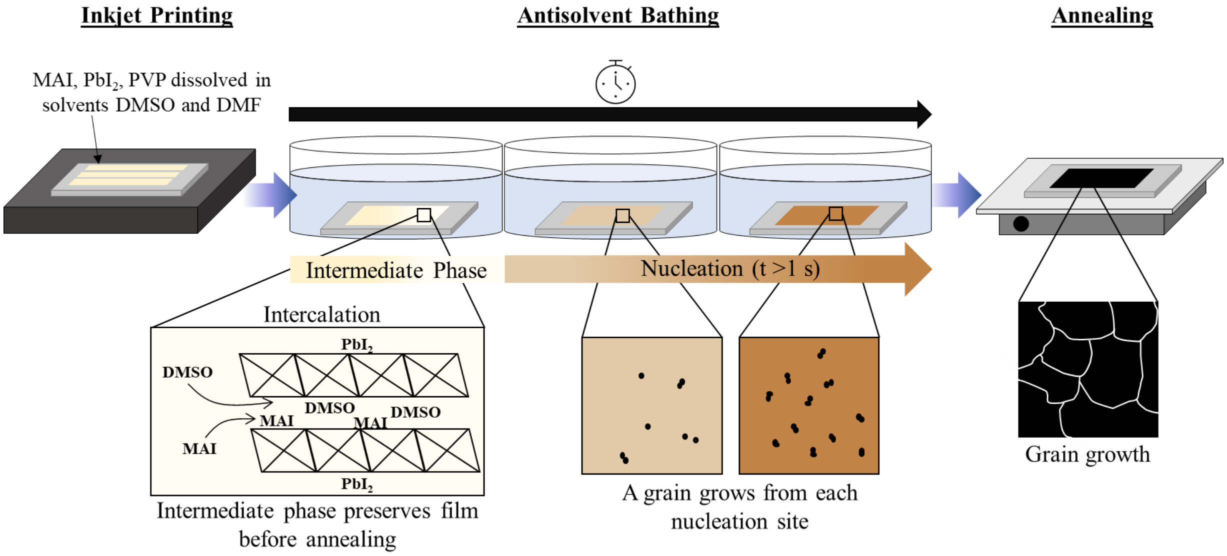

Figure 12. Perovskite Deposition, Intercalation, Nucleation, and Crystallization

5.2.1 Ink Rheology

Table 1. Rheology of Precursor Inks

	Concentration (mol solute/L solvent)	**Density** (g/mL)	**Viscosity** (mPa·s)	**Surface Tension** (mN/m)	**Oh.**	**Re.**
I1	2.86	1.51	4.3	33.1	12.7	62.3
I2	3.08	1.55	5.3	33.1	10.5	52.2
I3	3.33	1.62	6.3	33.3	9.0	46.1
I4	3.64	1.66	7.3	33.4	7.9	40.3
I5	4.00	1.70	8.3	33.5	7.0	36.6

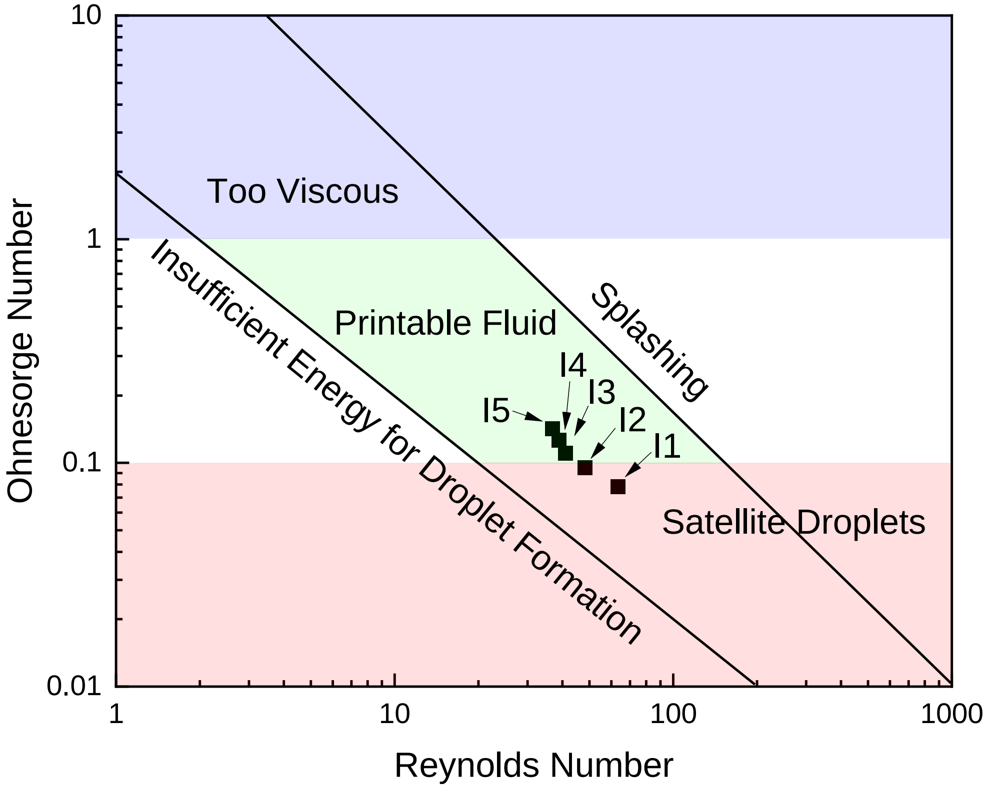

Figure 13. Printability of Precursor Solutions. Graph redrawn from Fig. 9a. Minor editing permission given by [50].

The rheology of the precursor ink was optimized primarily to fall within the constraints of the acceptable Ohnesorge number range. Density and viscosity were controlled by adjusting the total amount of binary solvent system (DMF and DMSO) in the ink, and thus the concentration. The five primary inks tested are labeled I1, I2, I3, I4, and I5. The concentrations and parameters related to the rheology of each precursor ink can be found in Table 1, which assumes a constant velocity and characteristic length of 3.0 $m \cdot s^{-1}$ and 0.6 µm, respectively. Throughout the optimization process, the ratio of DMF to DMSO, the 1:1 molar ratio of MAI and PbI_2, and the substrate preparation process were kept constant. Viscosity was measured using a rheometer, and surface tension was found using a drop shape analyzer. The Reynolds number was calculated using the average droplet velocity of around 3.0 m/s, which was measured by the printer's built-in camera. A waveform voltage of 30-33 V was found to provide sufficient energy for droplet generation.

As seen in Fig. 13, all the inks apart from I1 and I2 fell within the constraints of the Ohnesorge and Reynolds number range. I1 and I2 predictably produced satellite droplets upon ejection from the printhead, even at relatively low voltages. I5 suffered from insufficient spreading which resulted in a thickness gradient across the film, as seen by the dark and light-colored patches seen in Fig. 14. Scanning electron microscope (SEM) cross-sectional images revealed that the higher viscosity of I4 and I5 had trouble penetrating the mesoporous TiO_2 structure. As a result, many air pockets could be seen at the interface of m-TiO_2 and perovskite. Furthermore, these films had more pinholes and smaller grain sizes.

I3 and I2 were able to form a more uniform film, with no visible thickness gradient. These inks were also found to adequately penetrate the m-TiO_2 layer, which allowed for better interfacial contact. Both of these improvements are accredited to the lower viscosity of these inks.

The reduced current density of I5 compared to I3 is likely due to reduced charge extraction caused by the poor interface contact. The reduced voltage of I5 is likely caused by pinholes, which were present in the more viscous films. The pinholes could lower the shunt resistance in the device by creating avenues for electron-hole recombination. There was also reverse-forward IV scan hysteresis seen in I5 devices, which is likely due to the increased presence of grain boundaries, which act as defects or trap sites. The forward scan resulted in a lower efficiency, which is likely due to the fact that when the device is measured from a starting voltage of 0 V, trap sites are not yet filled, which inhibits carrier lifetime.

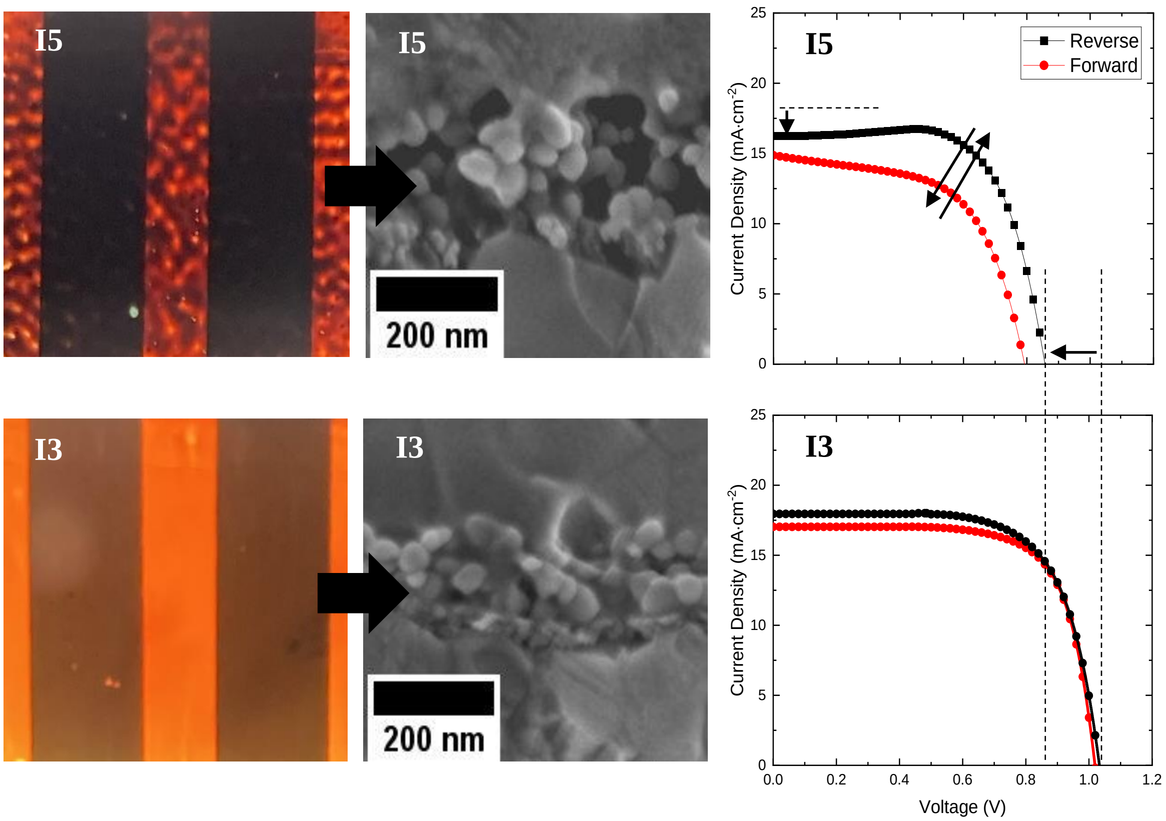

Figure 14. Implications of Poor Ink Spreading. Figure shows illuminated films (left), SEM cross-section image of perovskite-mesoporous TiO_2 interface (middle), and resulting JV curves (right).

5.2.2 Substrate Preparation

The surface energy of the substrate is an important parameter to optimize for the generation of uniform thin films with high resolution. Here, resolution refers to the sharpness of the edges and the representation of the indented shape. The surface energy was tuned by cleaning the substrates with a UV-Ozone generator. The longer the substrate was exposed to the O_3, the higher the surface energy was found to be. As seen in Fig. 15, it appeared that most of the change in substrate surface energy occurred within the first 5 minutes of treatment. UV-Ozone treatment times of 0, 5, and 15 minutes were tested to find the optimal degree of spreading. No UV-Ozone treatment resulted in limited droplet spreading and thus no thin film formation.

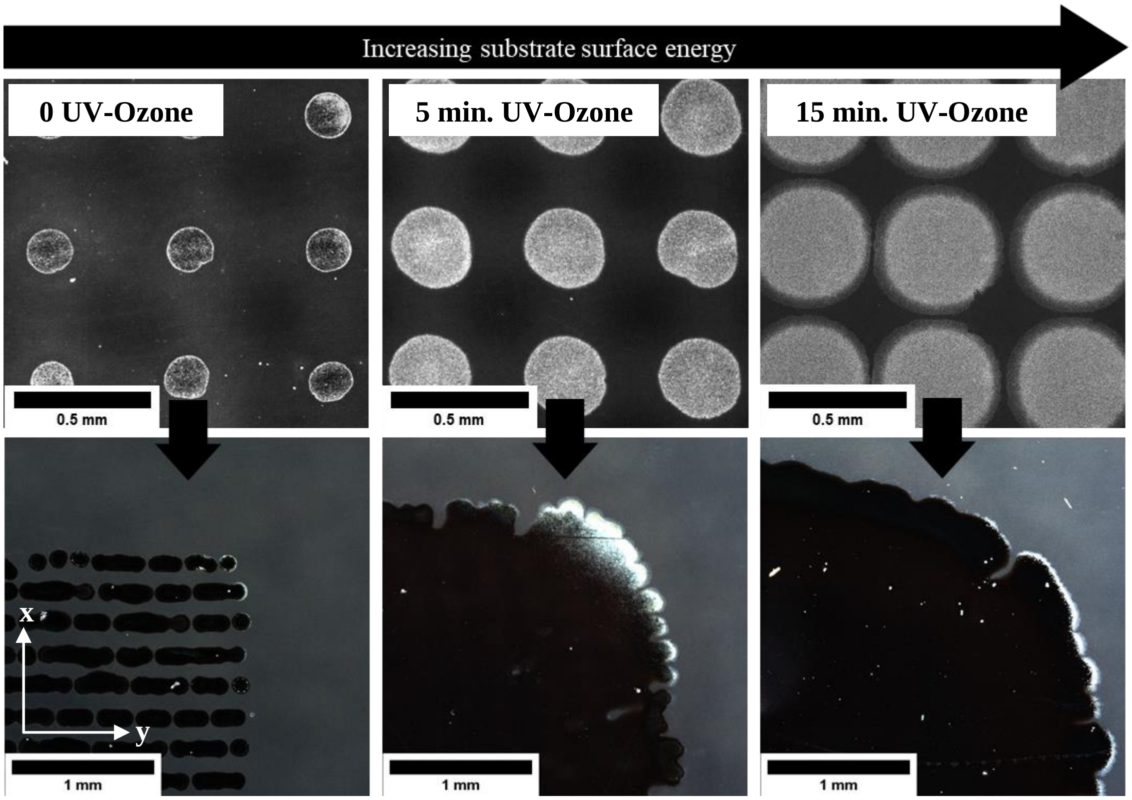

Figure 15. Effect of UV-Ozone Treatment on Ink Spreading. Drop spacing in top images are set to 0.5 mm in x and y-direction. Drop spacing in bottom images are set to 0.12 mm in x-direction, and 0.20 in y-direction.

A duration of 15 minutes resulted in low-resolution edges, due to excess spreading induced by the high surface energy. Finally, a UV-Ozone treatment time of 5 minutes was found to provide sufficient surface energy for droplet spreading, without excess uncontrolled fluid flow.

5.2.3 Printing Conditions

Just as substrate preparation and ink rheology have a large effect on the fluid flow of the ink, the print pattern was found to also be a relevant factor. It was found that when the drop spacing in the x and y direction (d_x, d_y) were the same, a larger mesoscopic flow arose predominantly in the direction of the printhead (d_y) due to the already-deposited ink tending to merge with the newly deposited ink droplets.

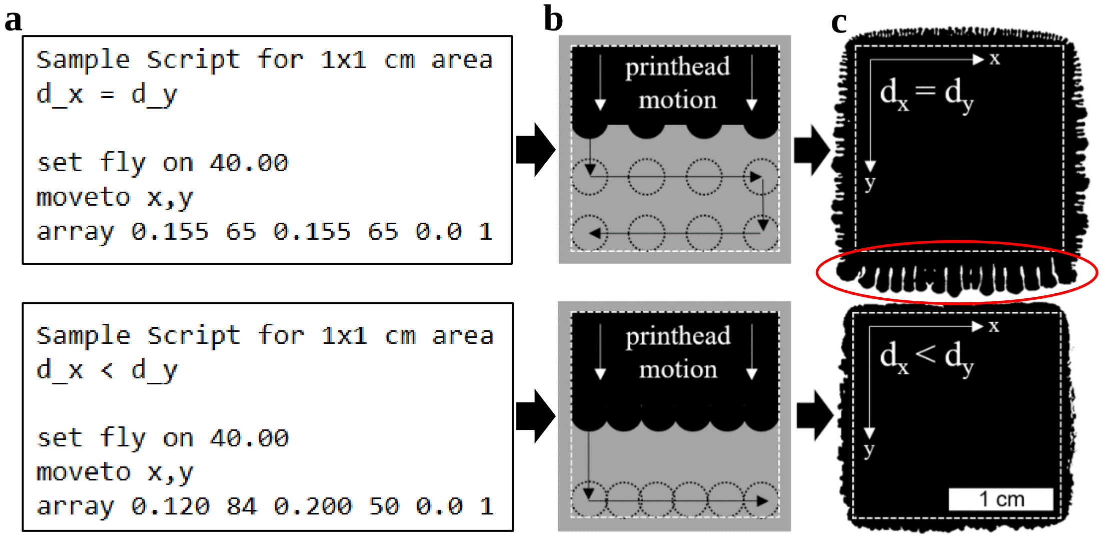

```
Sample Script for 1x1 cm area
d_x = d_y

set fly on 40.00
moveto x,y
array 0.155 65 0.155 65 0.0 1
```

```
Sample Script for 1x1 cm area
d_x < d_y

set fly on 40.00
moveto x,y
array 0.120 84 0.200 50 0.0 1
```

Figure 16. Effect of Printing Pattern on Ink Spreading. (a) Printing script, numbers in array represent drop spacing in dx, number of droplets along x, spacing in dy, number of droplets along y, angle about starting point, and bidirectional printing indication.

This causes a buildup of excess ink at the leading edge of the film, which grows as the print head deposits ink, as seen in Fig. 16c. Furthermore, a coffee ring effect, which describes the tendency for solute particles in a fluid to build up at the edges due to the constant replenishment from the bulk of the fluid, was observed. This was likely induced by excess capillary flow predominantly in the y-direction. To resolve this, the fluid flow had to be controlled. A new pattern with a large drop spacing in the y-direction and a small drop spacing in the x-direction was developed in an attempt to offset the excess fluid flow induced by the printhead motion. The uneven drop spacing encouraged isotropic fluid flow across the substrate by limiting the buildup of ink moving under and with the printhead. The results are seen in Fig. 16. Eventually, a drop spacing of 0.12 x 0.20 mm (d_x, d_y) was optimized for even spreading of the ink. The coffee ring effect also disappeared due to reduced capillary flow along the y-direction.

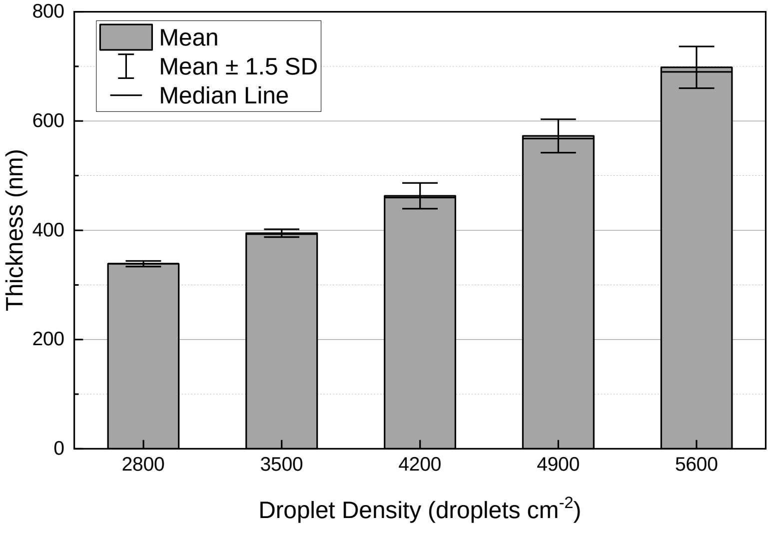

Figure 17. Film Thickness as a Function of Droplet Density.

A distinct advantage of inkjet printing is the ability to easily and precisely control the thickness of the film, which is directly related to the density of droplets and droplet volume. Fig.

17 shows empirical values of thicknesses obtained from SEM cross-sectional images. For these trials, the $d_x < d_y$ style drop spacing was used to limit spreading, which limited any thickness gradients induced by excess fluid flow. Thickness was measured from the TiO_2 blocking layer for consistency, and a thickness of around 450 nm was used as a target for all measured devices. It is worth noting that the larger deviation of thickness seen at larger droplet densities is representative of the loss of control that comes with more fluid on the substrate. These thick films are more susceptible to excess spreading and thus thickness gradients across the film, even with $d_x < d_y$ drop spacing. Thicker films were also found to be more likely to have pockets of air within the bulk, lowering the overall density of the film. In these cases, the film may be too thick for trapped pockets of air to escape during the solvent diffusion process.

5.2.4 Multi-Pass Printing

The final printing parameter to be tested was the effect of multiple passes of the printhead over the substrate on the uniformity and microstructure of the film. In this process, a first pass would form a uniform base film that the next pass could use as a guide for spreading. The process was optimized when the initial pass dropped roughly two-thirds of the ink, and a second pass dropped the remaining third. If the first pass dropped only half of the ink, evaporation of the film was too rapid, and the ink struggled to form a cohesive base layer. Overall, the multi-pass films looked similar to the single-pass films with the exception of an enhanced coffee ring effect, as seen in Fig. 18.

The proposed mechanism behind these observations is as follows: the first pass underwent more evaporation due to the smaller amount of total ink on the substrate. Since solvent from the edges of the film evaporates much faster than solvent from the bulk, a significant capillary flow was likely induced and carried the solute particles to the edges. The second pass of ink made this effect worse, as it acts as replenishment of fluid from the bulk of the film.

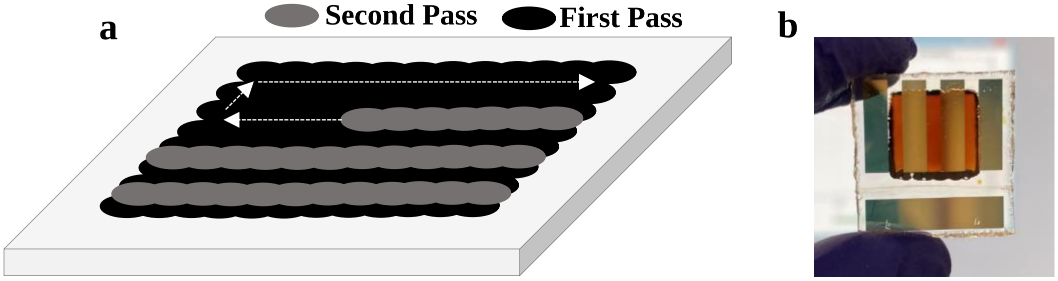

Figure 18. Multi-pass Printing. (a) Schematic of multi-pass printing. (b) Enhanced coffee ring effect.

Electrodes are evaporated in the center of the film, so excessively thick edges did not significantly affect the measurements. When comparing the same values of droplet density, the thickness of the multi-pass films was slightly less than the single-pass films, due to edges having a higher concentration of solute. This was offset by slightly increasing the droplet density to account for the coffee ring effect. Multi-pass printing was found to enhance many measured properties of the devices, including grain size. This is discussed further in section 5.5.

5.3 Effect of Mesoporous-TiO_2 Thickness

Since the interface between m-TiO_2 and perovskite is a crucial element in the operation of a perovskite solar cell, an experiment into the effect of the thickness of this layer was conducted. The thickness of the m-TiO_2 was altered by tuning the concentration of the m-TiO_2 in ethanol before spin coating. As seen in Fig. 19, an optimum thickness for the mesoporous m-TiO_2 was found to be at approximately 150 nm, which was achieved by depositing a solution with a ratio of m-TiO_2:ethanol (1:5.5, v:v). A steady increase in current and efficiency was identified with increasing m-TiO_2 thickness. Interestingly, voltage appeared to be steady throughout 0 and 150 nanometers of m-TiO_2, suggesting that the accumulation of voltage is not largely dependent on the m-TiO_2.

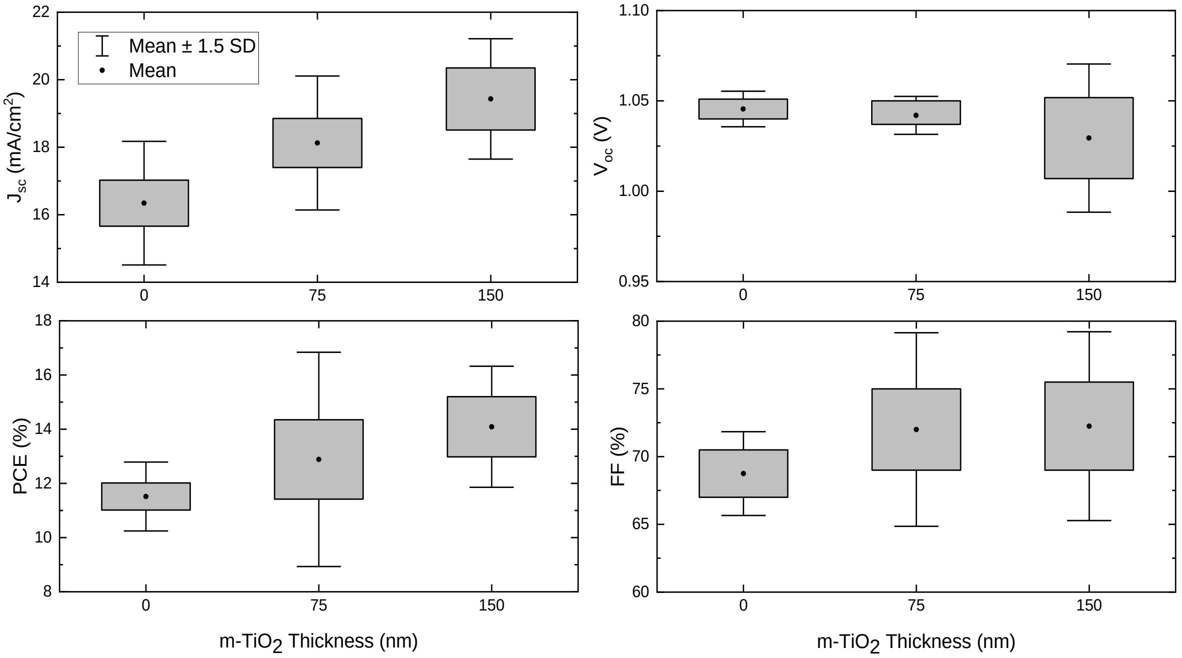

Figure 19. Statistical Analysis on the Effect of TiO_2 Thickness. Data representative of 8 samples, (16 electrode measurements).

The increase of J_{sc} in the devices with increasing m-TiO_2 appeared to be the only variable that significantly changed and is largely responsible for the similar trend observed in PCE. These improvements justify the use of mesoporous-TiO_2 as a means of enhancing charge extraction, due to the increased contact area between the two layers. No noticeable difference in perovskite spreading or film formation was observed with the changing m-TiO_2 thickness.

5.4 Solvent Engineering and Antisolvent Bathing

The optimization of the solvent system, which describes the ratio of solvents DMSO to DMF, and the antisolvent system, which describes the composition of the antisolvent (AS) bath, were done simultaneously. In section 5.4.1, it can be assumed all films were washed with the antisolvent diethyl ether. In section 5.4.2, the process of optimizing an antisolvent bath is discussed. In this section, where several antisolvents are compared, it can be assumed that the optimized volumetric ratio of 1:6.5 DMSO:DMF is kept constant. The two sections are dependent on each other, and a brief executive summary is found in table 3, at the end of section 5.4.2.

5.4.1 Solvent System

After an ink precursor concentration was established, a solvent system, which describes the ratio of solvents DMSO to DMF, had to be optimized for inkjet printing and antisolvent bathing. Three ratios of solute to total solvent were tested: 1:4, 1:6.5, and 1:8 (DMSO:DMF, v:v). It was found that the 1:4 ratio often resulted in hazy films. SEM images revealed that these hazy areas had a high density of pinholes. The hazy and non-reflective appearance of the films as seen in Fig. 20a is likely the result of light scattering caused by the discontinuities across the film. The pinholes also caused a reduction in voltage for these devices, as shunt resistance decreased due to current leakage. At the 1:4 ratio, which has a relativity large amount of DMSO, the antisolvent bath may not have been able to fully wash the DMSO away. The pinholes are likely the result of excess DMSO in the film, which upon thermal annealing, will evaporate and interrupt the grain growth process.

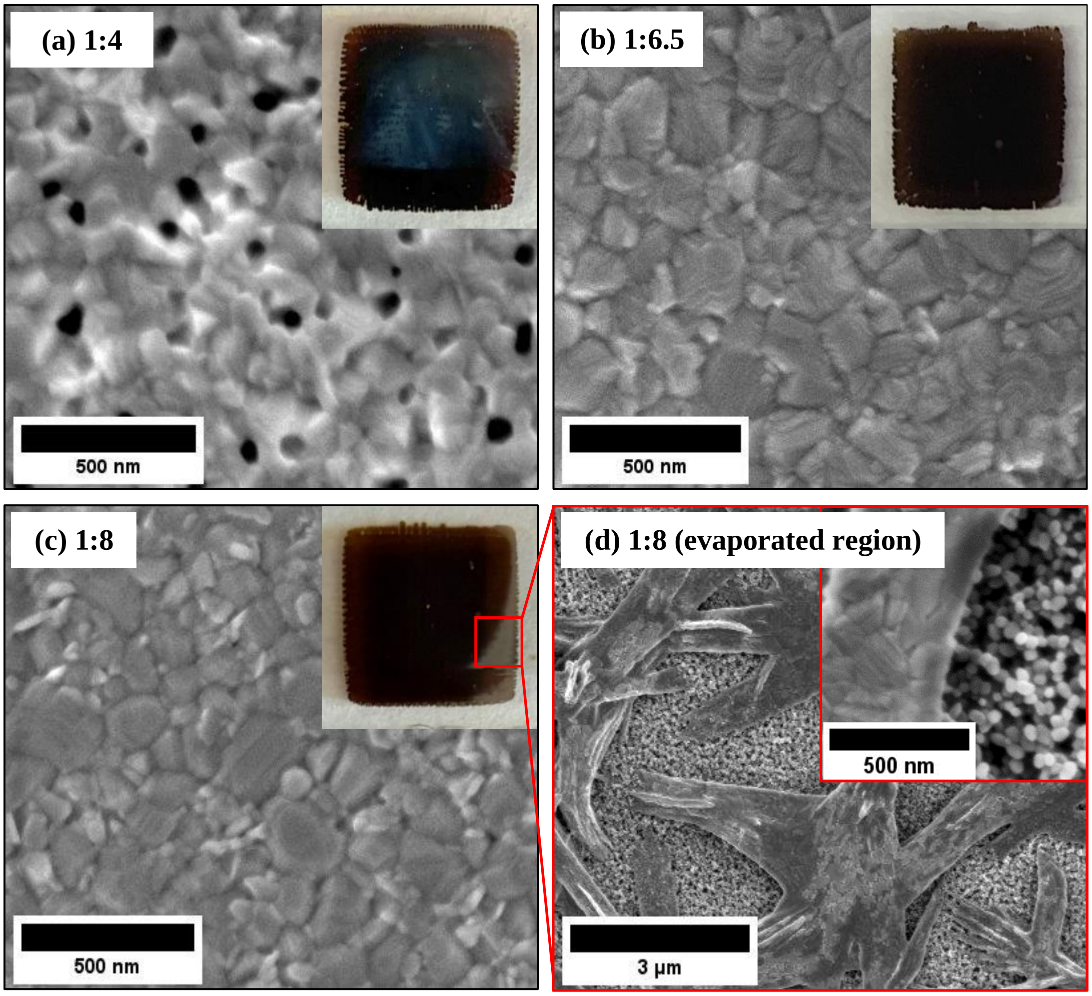

Figure 20. Effect of Solvent System on Microstructure. Ratios represent volumetric DMSO:DMF.

After this was repeatedly observed, a new solvent ratio of 1:8 was tested. This time, the films did not show any haze and were reflective and translucent, as seen in Fig. 20c. They did however suffer from excess evaporation of solvent from the edges before antisolvent could be applied. This is due to the higher vapor pressure of DMF, compared to DMSO. The film in this area does not form uniformly. Instead, large needle-like crystals of perovskite were formed on top of m-TiO_2. This is seen in Fig. 20d. The slow evaporation of DMF appeared to induce rapid anisotropic grain growth. This means that the concentration of the film at the edges, caused by evaporation of DMF, was below the critical concentration for facile nucleation, but above the concentration required for grain growth. It was observed that these crystals were made up of grains that were similar in size to the grains in the bulk of the film. These crystallization mechanisms will be discussed further in section 5.4.2.

A compromise between DMSO and DMF was made, and the solvent ratio of 1:6.5 was found to adequately preserve the film before antisolvent treatment, while also keeping it below the threshold for hazy films, as seen in Fig. 20b. This result highlights some limitations of a single nozzle system. The rapid evaporation of the 1:8 system would likely be avoided with a multiple printhead system, which would reduce the processing time by several orders of magnitude. The single nozzle setup took about 90 seconds to print a 1 cm^2 active area, which is roughly the time it takes for the 1:8 DMSO:DMF ink to begin to rapidly evaporate from the film edges. It should be noted that the performance of the 1:8 DMSO:DMF devices, which were tested in the middle of the film, was very comparable to that of the 1:6.5 DMSO:DMF. The grain size and structure also looked similar, suggesting that the middle of the film was not significantly affected by the evaporation at the edges.

5.4.2 Solvent Removal

The solvent system is just one part of the solvent engineering process. Solvent removal must too be optimized for each solvent system. First, vacuum-flashing was attempted. Vacuum-flashed films consistently showed poor morphology, as seen in Fig. 21. This was observed irrespective of the solvent system. Large spear-like structures on the scale of tens of microns covered the TiO_2 layers. The crystallized film was a matte gray color, which is attributed to light scattering caused by the rough film morphology. This film morphology was similar to that of the evaporated edges of the 1:8 DMSO:DMF solvent system, so it can be assumed that the same mechanisms described for the edges of the 1:8 DMSO:DMF film were relevant. This means the vacuum-flash system did not evaporate the solvents fast enough. Furthermore, this solvent removal method is not scalable, so after many failed attempts, it was decided not to further investigate this matter.

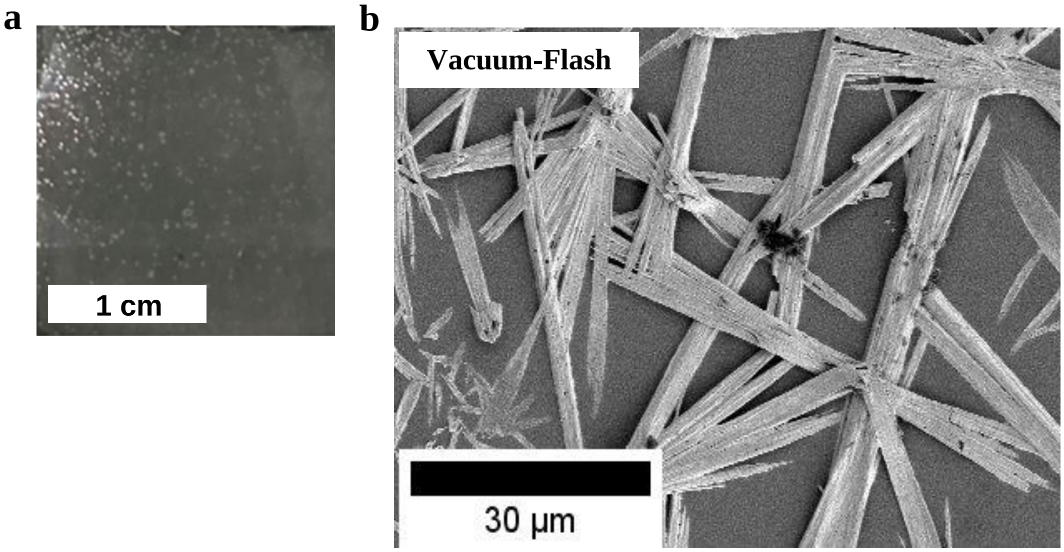

Figure 21. Vacuum Flashed Film. (a) Overhead picture of crystallized film. (b) SEM image showing long spear-like crystals grown on top of mesoporous TiO_2.

Antisolvent bathing was tested to replace vacuum flashing for the solvent removal step. This process was performed by immediately taking the perovskite-deposited substrate out of the printer and submerging it into a glass petri dish filled with the antisolvent. It was found that if the sample was moved with tweezers during submersion in the antisolvent bath, a more uniform diffusion was achieved. The motion of the antisolvent ensured a fresh supply of antisolvent across the film and eliminated DMF-rich spots that could develop in a stagnant bath. After taking the sample out of the bath, it was swiftly transferred to a hot plate to remove DMSO and crystallize the film.

The following antisolvent bath compositions were tested: A binary system of tert-butyl alcohol and ethyl acetate (t-BA:EA 7:3, v:v), ethyl acetate (EA), anisole (AN), and diethyl ether (DE). It should be noted that the t-BA:EA mixture was inspired by a previous result investigating antisolvent bathing of gravure-coated perovskite films. [7] DE, EA, and AN are common antisolvents used for antisolvent dripping.

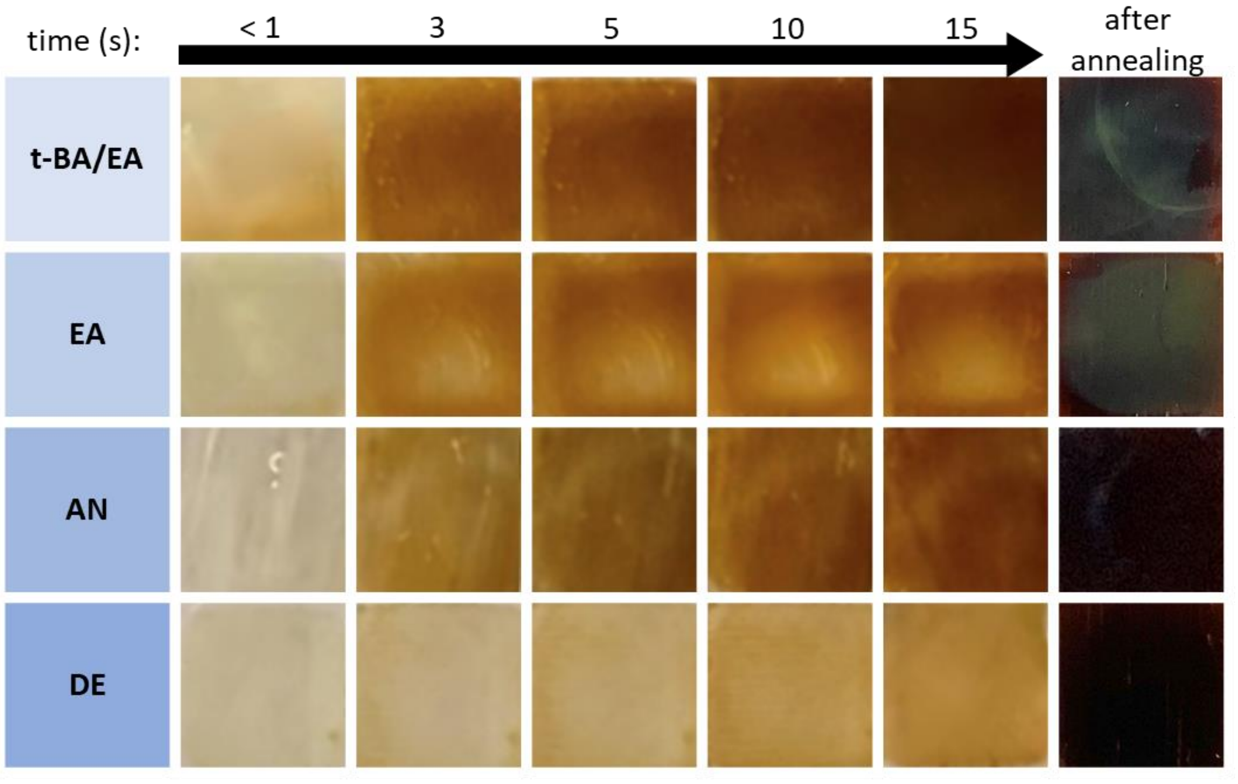

Figure 22. Antisolvent Bath Diffusion and Nucleation as a Function of Time. Pictures are frozen frames from an overhead camera. Rightmost column represents overhead pictures of crystallized films. t-BA:EA is tert-butyl alcohol:ethyl acetate (70:30, by volume).

Within a second of submerging the films into the antisolvent baths, the film turned from a yellow to white color. This indicated that the DMF is rapidly washed away, and thus the intercalation of MAI and DMSO into PbI_2 had occurred to form the intermediate phase. After a second or two, films began to burn brown at varying rates, indicating nucleation. As seen in Fig. 22, t-BA:EA, AN, and EA had relatively fast nucleation rates, while DE was slower. Despite the movement of antisolvent across the film, EA-bathed films resulted in bright and dark patches, which indicated uneven diffusion of solvents out of the film. After crystallization, all of the t-BA:EA and EA films were very hazy. The AN-bathed films were mostly reflective, but the DE-bathed films exhibited the highest degree of reflectance.

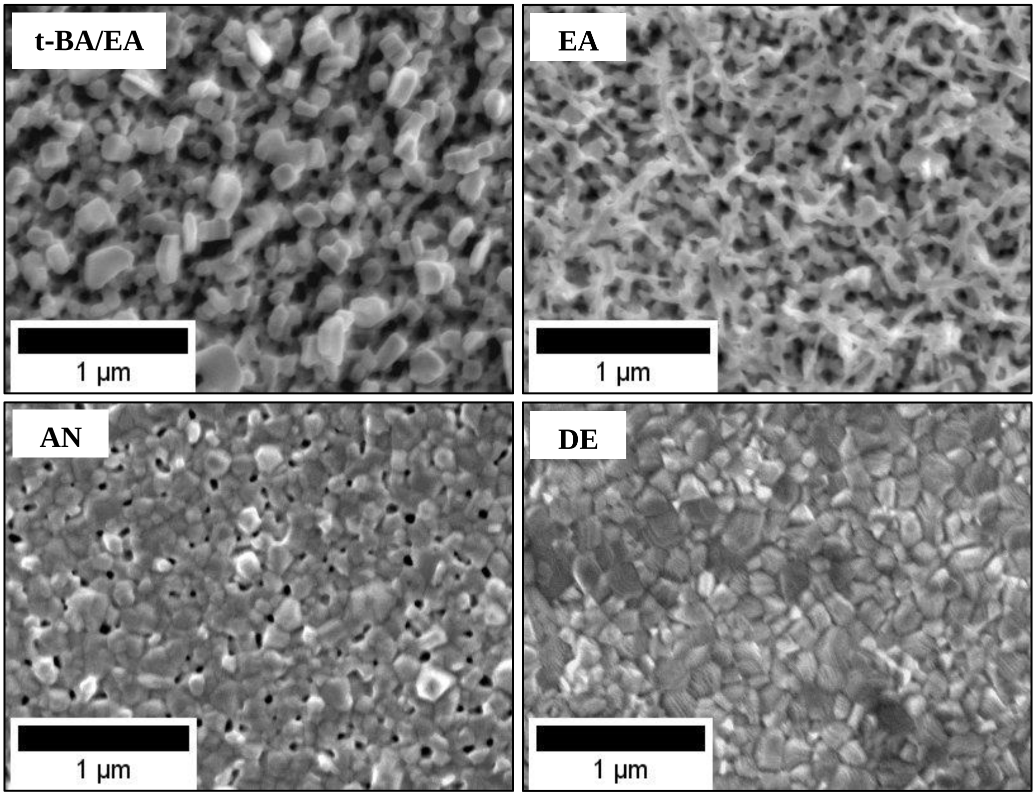

Figure 23. Scanning Electron Microscope (SEM) Overhead Images Showing the Effect of Antisolvent Bath Composition on Film Morphology.

Scanning electron microscopy (SEM) analysis was used to investigate film formation. As expected, the microstructure of t-BA/EA and EA were discontinuous. Films washed in t-BA:EA resulted in loosely packed grains with random orientation. EA produced short rod-like structures, also with low density. AN resulted in a drastically better grain structure, but pinholes were large and abundant. DE produced dense grains with very few pinholes. These results are seen in Fig. 23.

To decipher these results, it is important to understand what is happening in the antisolvent baths, and how it is related to the final morphology of the film. Table 2 lists the miscibility of the tested antisolvent with the solvents used in the precursor solution. The antisolvents in the first three rows are miscible with DMSO and DMF, which means that in the t-BA:EA, EA, and AN antisolvent baths, a large percentage of DMSO is likely washed away from the film, which could inhibit the formation of the MAI·PbI_2·DMSO intermediate phase. This means that rapid nucleation crystallization likely occurred unevenly throughout the film, which induced anisotropic crystal growth consistent with the SEM images as seen in Fig. 23. In the case of films washed with DE, the intermediate phase would form easier, because DE is not miscible with DMSO. This means that nucleation and crystallization were likely delayed, allowing the film to crystallize primarily in the annealing step. This supports the comparatively slow nucleation of DE seen in Fig. 22.

Table 2. Miscibility of Relevant Solvents and Antisolvents

	DMSO	**DMF**	**Film Result**
t-BA	miscible	miscible	discontinuous
EA	miscible	miscible	discontinuous
AN	miscible	miscible	pinholes
DE	**not miscible**	miscible	dense film

Another factor that can explain the poor morphology is the solubility of the antisolvents with the organic component, MAI. The t-BA:EA and EA were shown to easily dissolve MAI when simply mixed in a vile. This means that t-BA and EA may be dissolving some MAI during antisolvent bathing before it can convert to perovskite with PbI_2. The excess PbI_2, in this case, could explain the poor morphology.

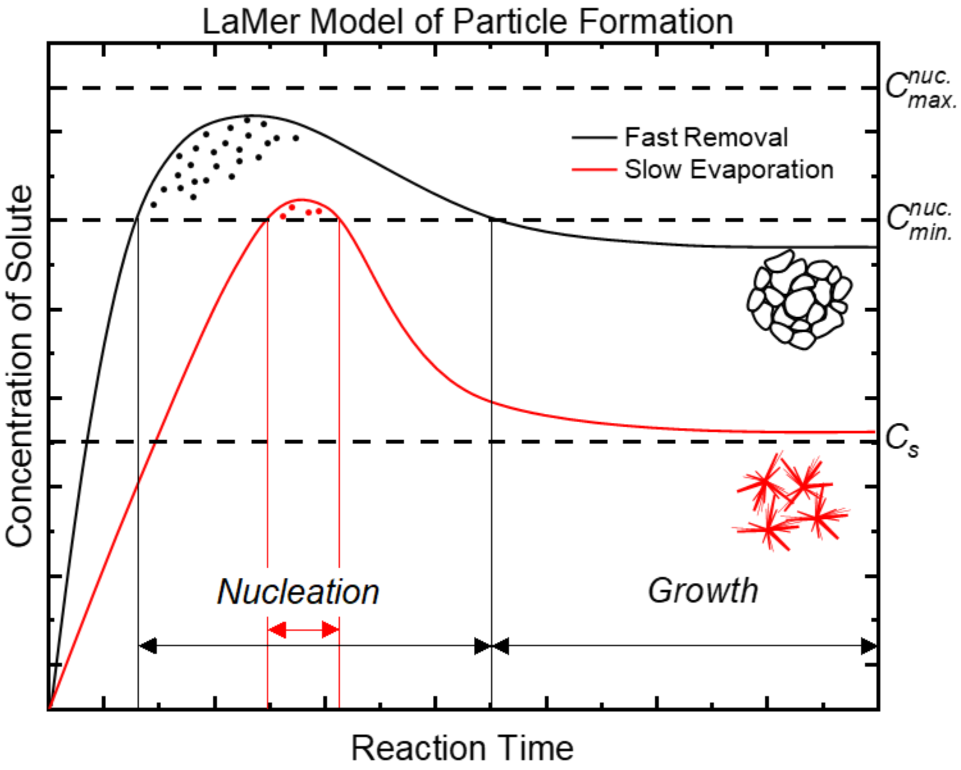

Figure 24. LaMer Model of Particle Formation. The lines represent the likely concentration of the films subjected to antisolvent and vacuum pressure over time. The dots represent nucleation sites. Final morphology is represented by schematics at the right edge.

It can clearly be seen that the antisolvent baths, despite having varying degrees of success in terms of forming dense films, all provide rapid solvent removal and nucleation, compared to vacuum flashing. The likely nucleation and growth kinetics of slow evaporation, provided by vacuum flashing, and fast removal, provided by antisolvent bathing, are plotted in Fig. 24. Antisolvent quickly overcomes the activation barrier for nucleation, which results in a high density of nucleation sites. The concentration begins to fall, as the rate of solvent removal is overcome by the rate of solute consumption for crystal growth. Assuming the intermediate phase is achieved, this results in densely packed films. In the case of slow solvent removal, the concentration of the film barely makes it above the critical concentration for nucleation. Because the concentration is low, grain growth rapidly ensues, which rapidly and drastically lowers the curve beneath the critical concentration for nucleation. This results in uncontrolled grain growth, as seen in Fig. 21.

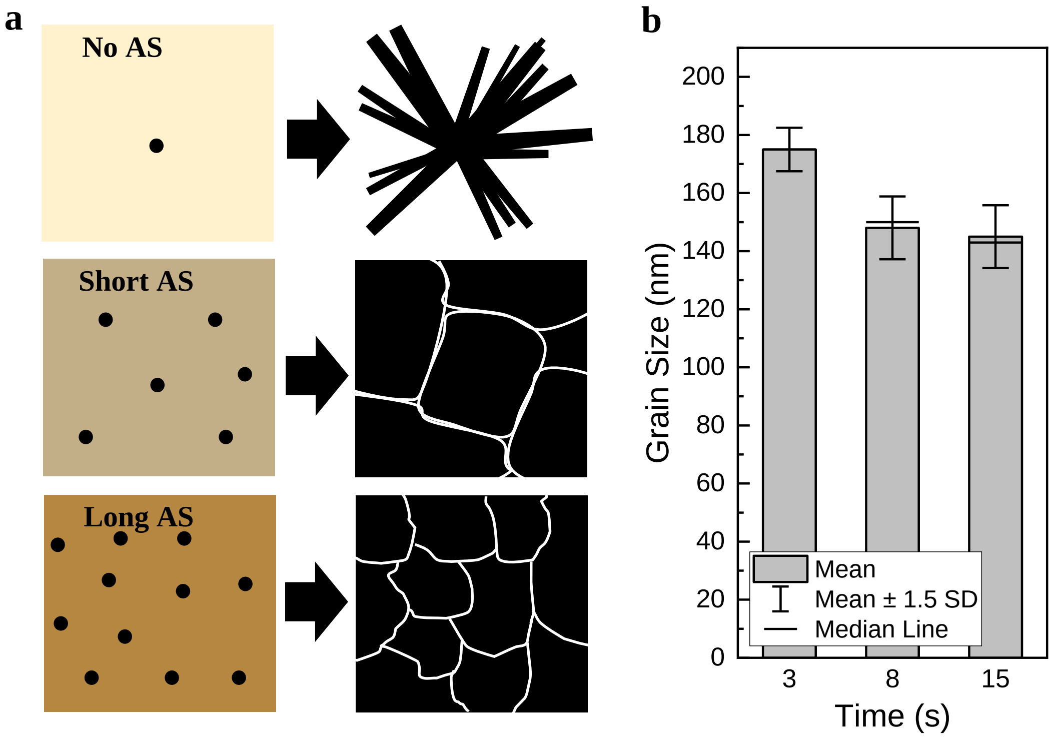

Figure 25. Effect of Antisolvent Bath Duration on Grain Size. (a) Black points represent nucleation sites. White lines represent grain boundaries. (b) Statistical analysis of grain size as a function of AS bathing time. Each bar represents the average of three films.

A follow-up study was designed in order to study the effect of DE antisolvent bathing time on the microstructure. There was very little change in film morphology from 3 to 15 seconds, apart from a slight increase in grain size. This could be explained by the density of nucleation sites, which is indicated by the color change in the film. Since each nucleation site grows into a grain, a lower density of sites would allow uninterrupted grain growth for a longer period of time. For a higher density of nucleation sites, each site would have less time to grow before running into another grain. This is visualized in Fig. 25a. There is a tradeoff between these two scenarios. High nucleation and smaller grain size typically resulted in very dense films with no discontinuities in between grains. Larger grains are favorable in terms of carrier lifetime but are more likely to have larger gaps in between grains, which would lower the device's shunt resistance.

The films appear to stabilize after around 8 seconds, with no statistically significant changes in grain size detected, as seen in Fig. 25b. This demonstrates a level of control that can be utilized using antisolvent bathing as opposed to conventional antisolvent dripping.

Table 3. Summary of Section 5.3. The appearance of films as a result of the solvent system and antisolvent composition. Ratios are volumetric.

	1:8	**1:6.5**	**1:4**
t-BA	Hazy/Pinholes	Hazy/Pinholes	Hazy/Pinholes
EA	Hazy/Pinholes	Hazy/Pinholes	Hazy/Pinholes
AN	Moderate/Pinholes	Moderate/Pinholes	Hazy/Pinholes
DE	Reflective/Dense	Reflective/Dense	Reflective/Dense

Table 3 summarizes this section. All devices measured from this point forward use a solvent system of DMSO:DMF 1:6.5 and use DE for solvent washing.

5.5 Addition of Polymers to Perovskite

The polymer polyvinylpyrrolidone (PVP) was chosen to study the effect of polymers in perovskite solar cells. PVP has good miscibility in DMF, and the C=O bonds in PVP are thought to have a synergistic attraction to the Pb^{2+} in $CH_3NH_3PbI_3$. [11][63] The molecular weight of 55 kDa was used. There are a few reports of the polymer PVP increasing the power conversion efficiency of PVP, but these reports are limited to spin coating deposition [63][67] and two-step spin coater-based processes. [11][8] Therefore, the possible implications of single and multi-pass one-step inkjet printing of perovskite-polymer films will be explored.

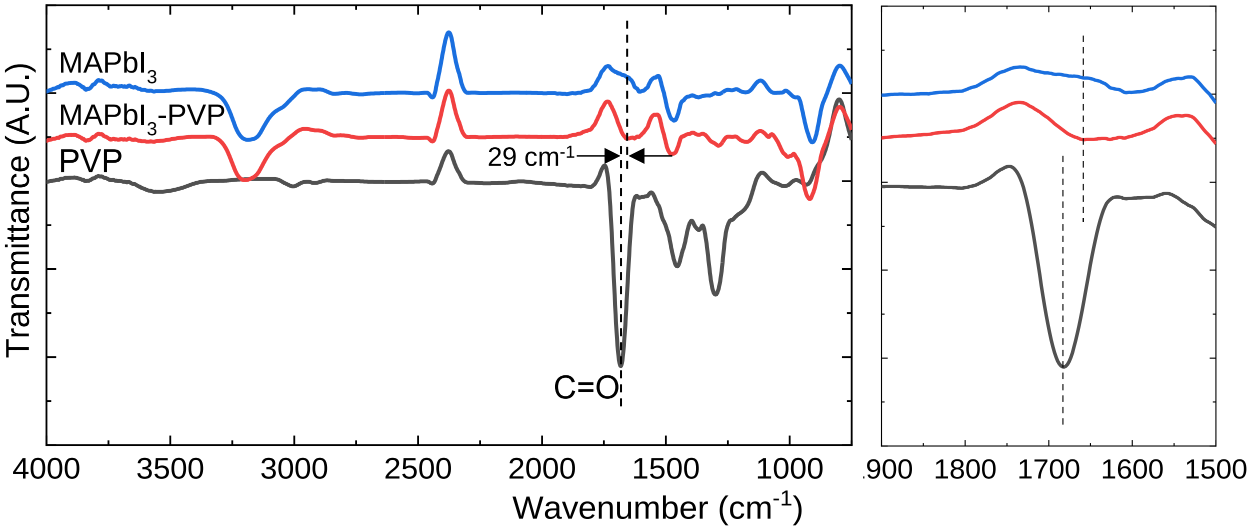

Figure 26. FTIR Spectrum of MAPbI$_3$-PVP, MAPbI$_3$, and PVP. Spectrum is baseline corrected and smoothed with a Savitzky-Golay filter (50 points of window).

Fourier Transform Infrared Spectroscopy (FTIR) measurements were taken to explore the interaction between perovskite and PVP, as seen in Fig. 26. The C=O bond vibrational peak was detected at 1681 cm^{-1}, as well as a dip in the $MAPbI_3$-PVP curve at 1652 cm^{-1}, indicating PVP-perovskite bonding. This shift of 29 cm^{-1} is likely due to the covalent coordination bond between the unbonded pair of electrons in O with Pb^{2+}. This confirms that the simple dissolving of powder PVP into precursor solution is an effective means of forming these adducts.

5.5.1 Effect of Polymers on Microstructure

Polyvinylpyrrolidone was added in the following amounts: 0.1, 0.2, 0.5, and 1.0 (wt.% of total precursor solution). First, the polymer composite inks were printed using the single-pass method. It was found that grain size decreased as the amount of polymer PVP increased, suggesting that the PVP slowed the rate of grain growth, allowing for a more densely packed film with smaller grains to grow.

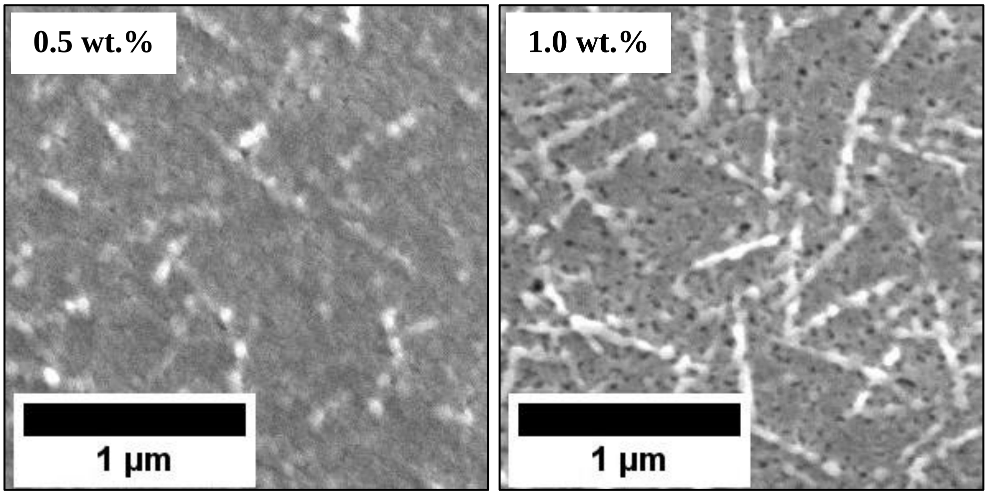

Figure 27. Scanning Electron Microscope Overhead Images of 0.5 and 1.0 wt.% PVP

White fringes began to appear in SEM images at 0.5 and 1.0 wt.% PVP, as seen in Fig. 27. These fringes are believed to be excess PVP that could not work their way into the perovskite grain boundaries. The number of pinholes also increased significantly as PVP was added after 0.2 wt.%, which likely added to the dramatic loss in current that was observed. These pinholes and discontinuities may have arisen due to the excessively sluggish grain growth rate caused by excessive polymer disruption. As seen in Fig. 29 (single-pass column), pinholes were not prevalent in 0 – 0.2 wt.% PVP films.

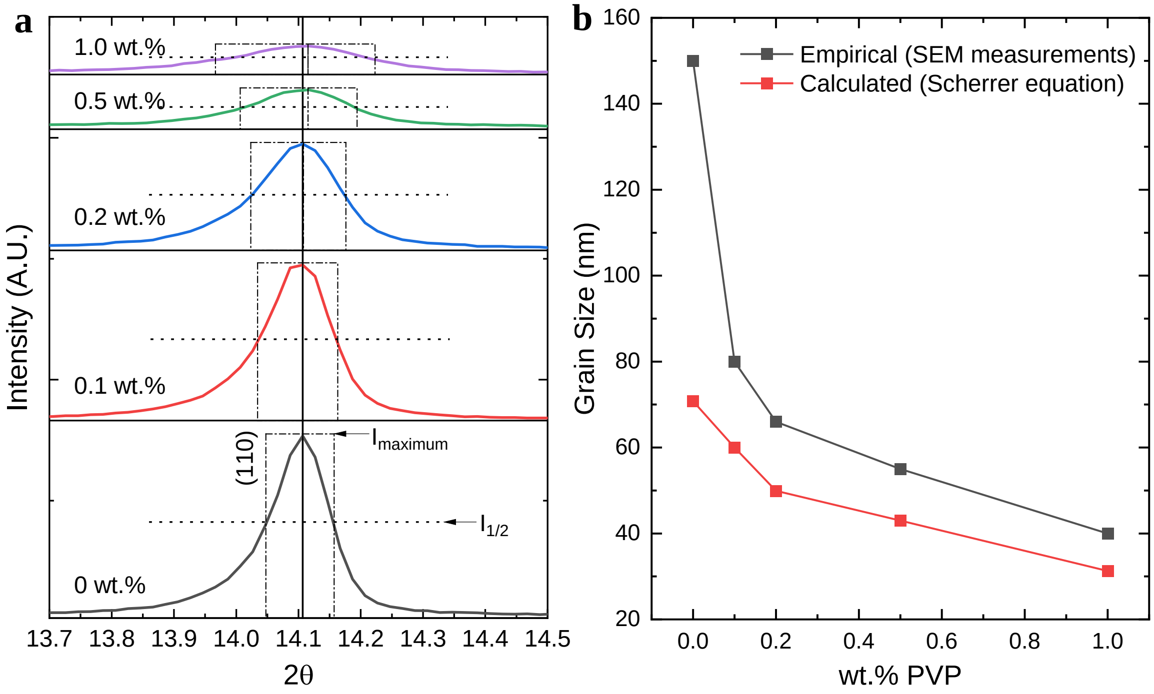

Figure 28. Broadening of Single Pass Films. (a) Half and maximum XRD intensity of the (110) peak. (b) Empirical (from SEM overhead images) and calculated (Scherrer equation) average grain size.

X-ray diffraction (XRD) also showed peak broadening of the (110) perovskite peak, as seen in Fig. 28a. The peak broadening could be attributed to the reduction in grain size. The empirical grain size obtained from SEM overhead images and theoretically calculated grain size from the Scherrer equation are compared in Fig. 28b. A similar trend between empirical and calculated grain size was observed, meaning that the broadness of the (110) peak accurately depicts the relationship between PVP and grain size for grains smaller than approximately 100 nm in diameter.

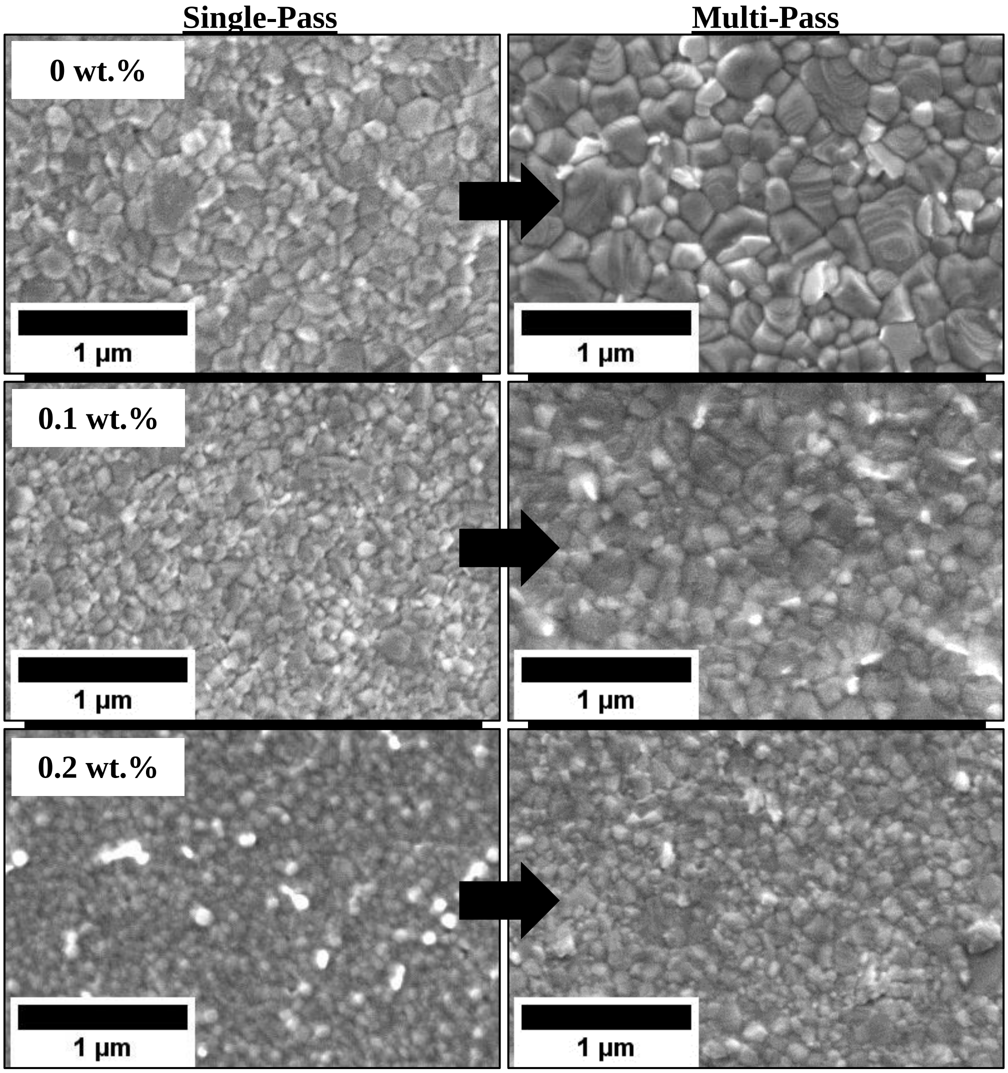

Figure 29. SEM Top-down Images Showing the Effect of PVP on Grain Size. The left column is single-pass. The right column is multi-pass.

The increasing broadness is indicative of the increasing presence of grain boundaries, which induce stress and strain across the film. Strain causes fluctuations in the diffraction angle and thus increases the peak width. Gradual shifting to larger Bragg angles was observed starting at 0.2 but was more noticeable in 0.5 and 1.0 wt.% PVP. This suggests that the strain is not evenly distributed and that there was a larger presence of compressional strain compared to tensile. This may be due to the polymer pushing against the grains from the grain boundaries.

Multi-pass printing was found to increase the grain size consistently, as seen in Fig. 29. From section 5.4.2, a relationship between the density nucleation sites and grain size was established. The same logic is thought to be the mechanism for the observed increase in grain size that resulted from multi-pass printing. It is proposed that in single-pass printing, many nucleation sites form before antisolvent treatment, due to DMF evaporation before antisolvent bathing. In the case of multi-pass printing, any nucleation sites or seed crystals that may have formed after the first pass are redissolved after the second pass.

As a result, the nucleation is suppressed until antisolvent bath treatment, resulting in fewer nucleation sites. It is simultaneously possible that the nucleation sites from the second pass are grown from nucleation sites from the first pass, which would result in a smaller number of origin points from which crystals grow. Fig. 30. summarizes these findings.

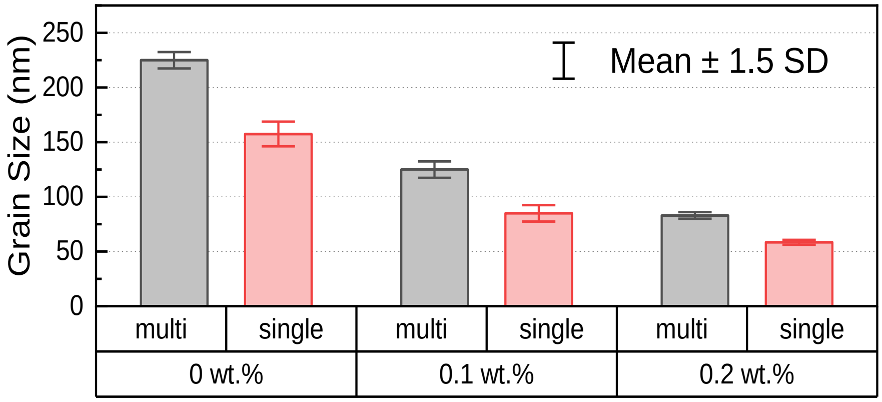

Figure 30. Effect of Printing Passes and Polymer wt.% on Grain Size. Each bar represents the average grain size from 3 films, obtained from SEM overhead images.

5.5.2 Effect of Polymer on Performance and Stability

A critical value was found in terms of performance of the PSCs, as seen in Fig. 31. Since the efficiency of the 0.5 and 1.0 wt.% films were so low, multi-pass devices were only made with 0, 0.1, and 0.2 wt.% PVP films.

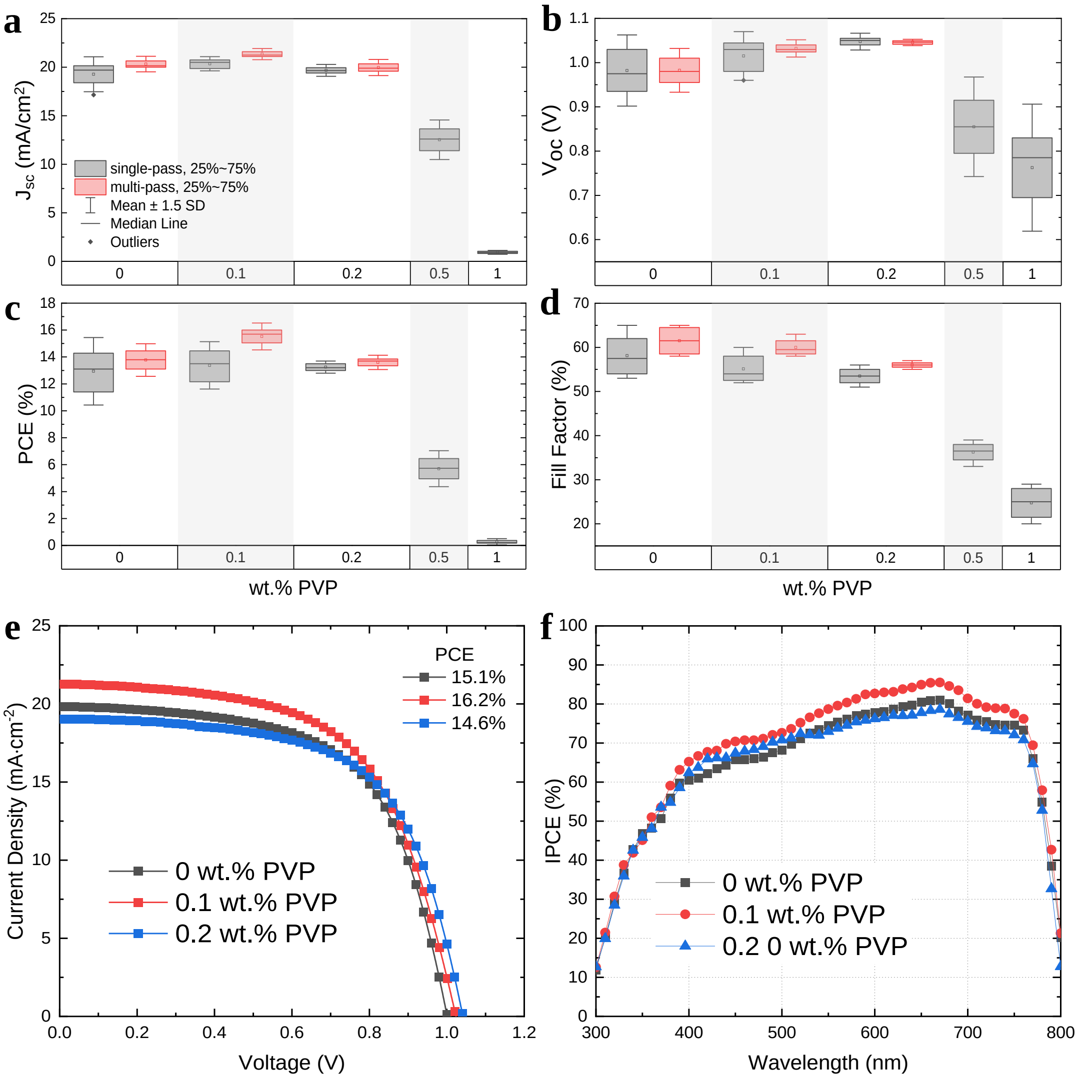

Figure 31. Effect of PVP on Performance. (a)-(d) Jsc, Voc, PCE, and FF with varying PVP. At least 5 devices were tested for each category. (e) Typical JV curves for 0, 0.1, and 0.2 wt.% PVP multi-pass devices. (f) Typical IPCE curves for 0, 0.1, and 0.2 wt.% PVP.

It was found that PVP steadily increased voltage, until a drop-off point was detected, between 0.2 and 0.5 wt.% PVP. In terms of short circuit current density and efficiency, a similar trend was noticed. Despite smaller grain size and increased presence of recombination hotspot grain boundaries, there was a slight increase, and then decrease, before and after 0.1 wt.% PVP. This was followed by a dramatic drop-off in between 0.2 and 0.5 wt.% PVP. Voltage was found to increase up until 0.2 wt.% PVP, which suggests that the small grain size in those films creates a very dense film, allowing for high shunt resistance. The multi-pass devices consistently performed similar or better than the single-pass devices, while also retaining a similar trend, in which the best performance was at 0.1 wt.% PVP. Despite the relatively large grains seen in the multi-pass control sample, the 0.1 wt.% PVP film recorded the highest average and overall champion PCE of 16.2 %. This demonstrates the effectiveness of grain boundary passivation.

The IPCE curves in Fig. 31f are relatively low for shorter wavelengths, implying more surface recombination at the front interfaces of the device. This implies there may be poor interfacial contact between the FTO and ETL, or ETL and perovskite, compared to the HTL and perovskite.

A 30-day time study was conducted to understand the degree to which polymers can preserve perovskite films. During the 30 days, the solar cells were kept in ambient conditions, near a window. The average humidity during the study was 23%, and an average temperature of around 22°C was maintained. The electrodes of the solar cells were reinforced with copper tape and silver paste after the gold electrodes began to develop holes due to repeated testing over the 30-day trial. PCE measurements were taken at each electrode and then averaged, to account for uneven degradation of the film. Pictures were also taken throughout the process to document the visual change in the films.

About 10 days into the study, all the films began to lose their reflective appearance. Eventually, separation of the perovskite into its component precursors of MAI and PbI_2 was observed, made obvious by PbI_2's distinct yellow hue, as seen in Fig. 32b. The control film showed the most yellow after 30 days, and a general trend of decreasing PbI_2 could be identified with increasing polymer content. The multi-pass films exhibited greater stability compared to their respective single-pass films. As seen in Fig. 32a, the multi-pass 0.1 and 0.2 wt.% devices maintained 73% and 78% of their original PCE over 30 days, respectively, compared to the control which only retained 23%.

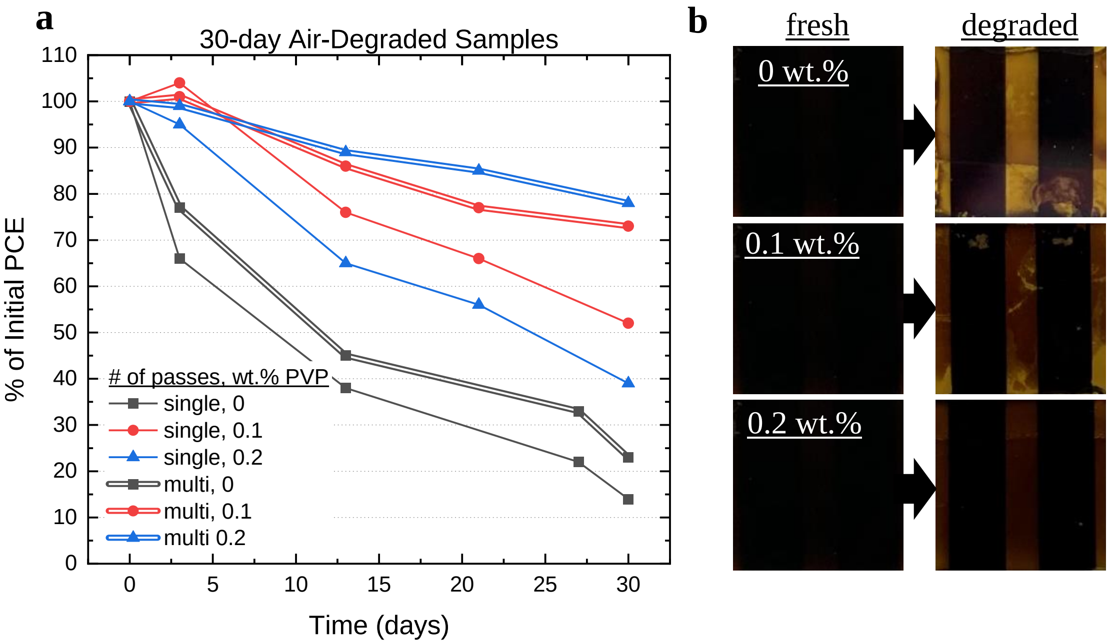

Figure 32. Stability of Perovskite-Polymer Devices in Ambient Environment. (a) 30-day time study. Each point represents the average losses of at least 3 devices. (b) Pictures of multi-pass fresh (left column) and 30-day degraded (right column). Yellow color indicates PbI_2, breakdown of $MAPbI_3$.

XRD measurements were taken initially and again after 30 days to further characterize the degree of degradation. It should be noted that the XRD patterns in Fig. 33 are all single-pass films.

It was found that the intensity of the characteristic (110) and (220) perovskite peaks in the fresh films was somewhat inversely proportional to the amount of PVP added into the film. Also, after 30 days, many of the (220) peaks broadened and shifted to smaller diffraction angles.

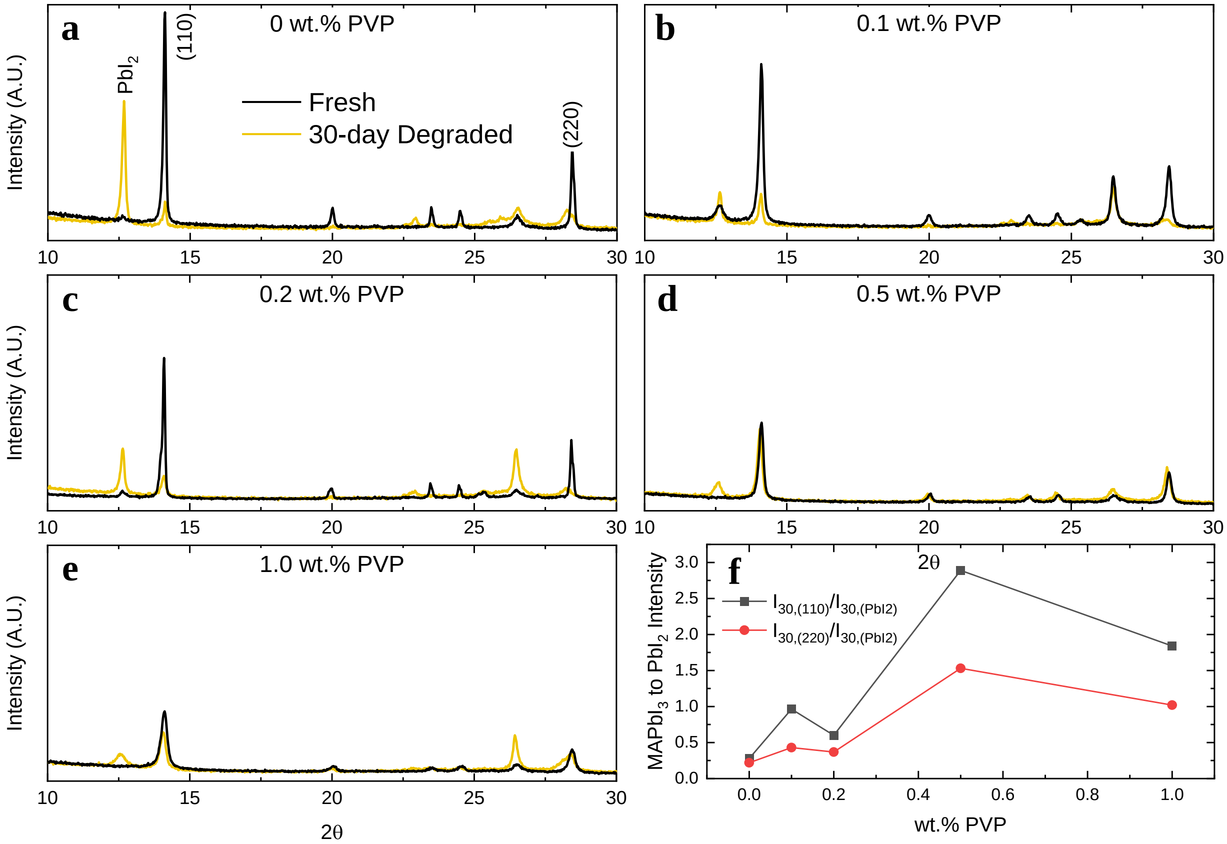

Figure 33. X-ray Diffraction (XRD) Spectra of Fresh and 30-day Degraded Single-Pass Films. (a)-(e) Black line represents fresh films. Yellow line represents degraded film. (f) Intensity ratio of 30-day degraded perovskite ((110) and (220)) to PbI_2 peak as a function of time.

The loss of (110) and (220) intensity in the fresh films suggests that a degree of crystallinity or long-range order in the film was lost with increasing polymer content. This can be explained by the increased presence of PVP in the films, and thus the lower concentration of perovskite. After 30 days, the intensity of these peaks decreased, and the PbI_2 peak increased, indicating the breakdown of perovskite into its precursor components. The intensity ratio of the degraded perovskite (110) and (220) peaks to the degraded PbI_2 peak is summarized in Fig. 33f. In the case of 0, 0.1, and 0.2 wt.% PVP films, the intensity of the PbI_2 peak became greater than the intensity of the (110) and (220) peaks after 30 days. Only the 0.5 and 1.0 wt.% films exhibited a greater presence of perovskite after 30 days, but at the expense of every other parameter that makes a solar cell efficient.

The shifting of the degraded perovskite (220) peaks is indicative of increased tensile strain in the lattice. The likely formation of hydrate products may be the driving force for this strain, but not much is known about the way in which they induce stress on the film. The FTO peak at 26.5° is also seen to increase in the degraded samples at every value except for 0.1 wt.% PVP. This suggests that as the film breaks down, it becomes discontinuous, allowing for x-rays to pass through and detect FTO. These XRD and PCE results indicate that polymers can be used to enhance the stability of perovskite solar cells despite the smaller grain size that they appear to induce.

6.0 Discussion and Future Work

Many factors affect the spreading and film formation of perovskite precursor ink on a substrate, all of which can influence the uniformity and eventual formation of the polycrystalline film. The printing pattern, printing parameters, ink rheology, and substrate preparation must all be balanced to find a compromise between uniformity and resolution. To achieve this balance, we suggest that first, the rheology of the ink should be optimized for inkjet printing. Next, the other parameters such as substrate preparation and printing pattern should be specifically tuned to accommodate that rheology. Since a certain degree of spreading is necessary for droplets to merge and form a continuous film, the resolution of the edges can only be so high. The resolutions in this work could likely have been improved with a smaller printhead orifice since the orifice diameter is related to droplet size. Most reports of inkjet printing perovskite films use a smaller orifice of around 20 μm in diameter. The printhead used in these experiments had a diameter of 60 μm.

Multi-pass printing shows promise for controlling grain size. If nucleation sites could be even further suppressed before antisolvent bathing, a significant increase in grain size could be expected. It could be interesting to see the impact of delay time between passes, or even the effect of three or more passes.

Clogging of the printhead was a notable problem throughout the research process and may threaten the practicality of inkjet printing. Filtering the ink through a PTFE filter helped reduce the likelihood of this, but when processing in an open, ambient environment, there is always a high risk of contaminants entering the printhead assembly and making their way to the printhead tip. Trials were done in small batches, which required frequent refilling of the ink reservoir. In a more dedicated environment, where only one ink is printed and sealed in a reservoir, clogging would likely be reduced. Internal filters placed between the ink reservoir and printhead can also reduce this risk. No internal filters were used in these experiments.

While vacuum flashing has proven to be a popular method for the extraction of solvents from an inkjet printed perovskite film, we do not believe that it is a viable option for high throughput operations. Furthermore, the results from the vacuum trials consistently resulted in highly discontinuous films, which suggested evaporation was too slow. While it is not well documented, the successful vacuum flashing reports likely used higher strength vacuum pumps, a tool that was not available at the time of these experiments. Even still, we did not believe it was worth pursuing this investigation further.

Antisolvent bathing can be integrated into the continuous processing method known as roll-to-roll, if flexible substrates could be continuously passed under and through printheads, antisolvent baths, and furnaces. As previously noted, a similar process has been done using gravure printing. [7] Future research in inkjet printing should focus on the development of scalable methods for solvent removal and intermediate phase generation. Optimizing antisolvent conditions such as temperature, fluid motion, and duration should be further studied to optimize the process.

Future research in perovskite-polymer composite films should partly focus on increasing the grain size of the composite films. It was demonstrated that inkjet printing can offer more control over grain size and film formation due to the ability to deposit multiple passes of ink. This observation should be further studied so that the potential for perovskite-polymer devices to be fully realized. While this study only focused on one polymer, it would be interesting to document which polymers have increased grain size, and which have not. If no consistent patterns are observed, it may be more likely that an increase or decrease in grain size is process-dependent. Currently, it is difficult to assume these potential relationships with the small number of studies that have been conducted in this field. Moreover, most studies have only investigated one or two polymers at a time.

Of course, the perovskite-polymer method and similar approaches such as using triple cation perovskite analogs are primarily explored to increase the internal or intrinsic stability of the film. Neither of these approaches would be completely effective with direct exposure to water. Polymers for perovskite solar cell encapsulation is a crucial, yet under-researched field. Polymer films, as opposed to glass, would allow PSCs to maintain their flexibility, translucence, and thin-film status. We believe that internal polymers, paired with a rigid, flexible, and highly hydrophobic external polymer encapsulation would create a robust system that could substantially increase the operating lifetime of perovskite solar cells.

7.0 Conclusion

To address the scalability and stability of perovskite solar cells, an innovative inkjet printing and antisolvent bathing process was utilized for the perovskite deposition and solvent removal. The spreading and uniformity of the thin film were found to be reliant on numerous factors relating to printing parameters, substrate surface energy, and ink rheology. A concentration of 3.33 mol/L was easily printable and adequately spread out over the substrate.

A volumetric ratio of 1:6.5 DMSO:DMF was found to preserve the film during printing and paired well with diethyl ether antisolvent. SEM analysis suggested that in order to achieve dense, pinhole-free film formation, the antisolvent must not be miscible with the coordinating DMSO solvent. Poor film formation was primarily attributed to antisolvents that washed DMSO out of the film before the intermediate phase could form. The solubility of MAI with certain antisolvents can also explain poor morphology. Short antisolvent bathing times and multi-pass printing were utilized to reduce the density of nucleation sites prior to grain growth, which could explain the increase in grain size from films processed in that manner.

PVP was shown to enhance the stability and efficiency of devices. In terms of performance, 0.1 wt.% PVP was found to work the best, resulting in a PCE of 16.2%. The increase of current density and efficiency in devices containing 0.1 wt.% PVP suggests that polymer additives can increase carrier lifetime despite polymers inducing smaller grain size. This suggests that grain boundaries are well passivated. Regarding stability, XRD analysis showed that the 0.5 wt.% films exhibited the smallest amount of degradation. Even still, the 0.1 wt.% multi-pass films retained 73% of their original PCE over 30 days in ambient conditions, compared to 23% from the control multi-pass device. We believe that these findings are valuable to the continuous pursuit of scaling up the production of perovskite solar cells.

Bibliography

[1] F. Mathies, H. Eggers, B. S. Richards, G. Hernandez-Sosa, U. Lemmer, and U. W. Paetzold, “Inkjet-Printed Triple Cation Perovskite Solar Cells,” *ACS Applied Energy Materials*, vol. 1, no. 5, pp. 1834–1839, May 2018, doi: 10.1021/acsaem.8b00222.

[2] Z. Li *et al.*, “Ink Engineering of Inkjet Printing Perovskite,” *ACS Applied Materials and Interfaces*, vol. 12, no. 35, pp. 39082–39091, Sep. 2020, doi: 10.1021/acsami.0c09485.

[3] C. Liang *et al.*, “One-Step Inkjet Printed Perovskite in Air for Efficient Light Harvesting (Solar RRL 2⁄2018),” *Solar RRL*, vol. 2, no. 2, p. 1770150, Feb. 2018, doi: 10.1002/solr.201770150.

[4] F. Schackmar *et al.*, “Perovskite Solar Cells with All-Inkjet-Printed Absorber and Charge Transport Layers,” *Advanced Materials Technologies*, vol. 6, no. 2, Feb. 2021, doi: 10.1002/admt.202000271.

[5] H. Eggers *et al.*, “Inkjet-Printed Micrometer-Thick Perovskite Solar Cells with Large Columnar Grains,” *Advanced Energy Materials*, vol. 10, no. 6, Feb. 2020, doi: 10.1002/aenm.201903184.

[6] B. Dou *et al.*, “Roll-to-Roll Printing of Perovskite Solar Cells,” *ACS Energy Letters*, vol. 3, no. 10, pp. 2558–2565, Oct. 2018, doi: 10.1021/acsenergylett.8b01556.

[7] Y. Y. Kim *et al.*, “Roll-to-roll gravure-printed flexible perovskite solar cells using eco-friendly antisolvent bathing with wide processing window,” *Nature Communications*, vol. 11, no. 1, Dec. 2020, doi: 10.1038/s41467-020-18940-5.

[8] L. Zuo *et al.*, “Polymer-modified halide perovskite films for efficient and stable planar heterojunction solar cells,” 2017. [Online]. Available: https://www.science.org

[9] C. Y. Chang *et al.*, “Tuning perovskite morphology by polymer additive for high efficiency solar cell,” *ACS Applied Materials and Interfaces*, vol. 7, no. 8, pp. 4955–4961, Mar. 2015, doi: 10.1021/acsami.5b00052.

[10] S. Wang *et al.*, “Polymer strategies for high-efficiency and stable perovskite solar cells,” *Nano Energy*, vol. 82. Elsevier Ltd, Apr. 01, 2021. doi: 10.1016/j.nanoen.2020.105712.

[11] M. Zhong, L. Chai, Y. Wang, and J. Di, “Enhanced efficiency and stability of perovskite solar cell by adding polymer mixture in perovskite photoactive layer,” *Journal of Alloys and Compounds*, vol. 864, May 2021, doi: 10.1016/j.jallcom.2021.158793.

[12] A. Fakharuddin *et al.*, “Perovskite-Polymer Blends Influencing Microstructures, Nonradiative Recombination Pathways, and Photovoltaic Performance of Perovskite Solar

Cells," *ACS Applied Materials and Interfaces*, vol. 10, no. 49, pp. 42542–42551, Dec. 2018, doi: 10.1021/acsami.8b18200.

[13] T. H. Han *et al.*, "Perovskite-polymer composite cross-linker approach for highly-stable and efficient perovskite solar cells," *Nature Communications*, vol. 10, no. 1, Dec. 2019, doi: 10.1038/s41467-019-08455-z.

[14] U. Energy Information Administration, "International Energy Outlook 2019," 2019. [Online]. Available: www.eia.gov/ieo

[15] J. Cook *et al.*, "Consensus on consensus: A synthesis of consensus estimates on human-caused global warming," *Environmental Research Letters*, vol. 11, no. 4, Apr. 2016, doi: 10.1088/1748-9326/11/4/048002.

[16] H. Ritchie and M. Roser, "CO_2 and Greenhouse Gas Emissions," 2020. https://ourworldindata.org/emissions-by-sector (accessed Mar. 11, 2022).

[17] National Renewable Energy Laboratory (NREL), "Reference Air Mass 1.5 Spectra." https://www.nrel.gov/grid/solar-resource/spectra-am1.5.html (accessed Mar. 11, 2022).

[18] P. Calado *et al.*, "Evidence for ion migration in hybrid perovskite solar cells with minimal hysteresis," *Nature Communications*, vol. 7, Dec. 2016, doi: 10.1038/ncomms13831.

[19] B. Chen, M. Yang, S. Priya, and K. Zhu, "Origin of J-V Hysteresis in Perovskite Solar Cells," *Journal of Physical Chemistry Letters*, vol. 7, no. 5. American Chemical Society, pp. 905–917, Mar. 03, 2016. doi: 10.1021/acs.jpclett.6b00215.

[20] A. R. Chakhmouradian and P. M. Woodward, "Celebrating 175 years of perovskite research: A tribute to Roger H. Mitchell," *Physics and Chemistry of Minerals*, vol. 41, no. 6. Springer Verlag, pp. 387–391, 2014. doi: 10.1007/s00269-014-0678-9.

[21] W. A. Saidi and J. J. Choi, "Nature of the cubic to tetragonal phase transition in methylammonium lead iodide perovskite," *Journal of Chemical Physics*, vol. 145, no. 14, Oct. 2016, doi: 10.1063/1.4964094.

[22] P. S. Whitfield *et al.*, "Structures, Phase Transitions and Tricritical Behavior of the Hybrid Perovskite Methyl Ammonium Lead Iodide," *Scientific Reports*, vol. 6, Oct. 2016, doi: 10.1038/srep35685.

[23] H. Jin *et al.*, "It's a trap! on the nature of localised states and charge trapping in lead halide perovskites," *Materials Horizons*, vol. 7, no. 2. Royal Society of Chemistry, pp. 397–410, Feb. 01, 2020. doi: 10.1039/c9mh00500e.

[24] S. de Wolf *et al.*, "Organometallic halide perovskites: Sharp optical absorption edge and its relation to photovoltaic performance," *Journal of Physical Chemistry Letters*, vol. 5, no. 6, pp. 1035–1039, Mar. 2014, doi: 10.1021/jz500279b.

[25] H. F. Haneef, A. M. Zeidell, and O. D. Jurchescu, “Charge carrier traps in organic semiconductors: A review on the underlying physics and impact on electronic devices,” *Journal of Materials Chemistry C*, vol. 8, no. 3. Royal Society of Chemistry, pp. 759–787, 2020. doi: 10.1039/c9tc05695e.

[26] Q. Lian *et al.*, “Using Soft Polymer Template Engineering of Mesoporous TiO2Scaffolds to Increase Perovskite Grain Size and Solar Cell Efficiency,” *ACS Applied Materials and Interfaces*, vol. 12, no. 16, pp. 18578–18589, Apr. 2020, doi: 10.1021/acsami.0c02248.

[27] A. Kojima, K. Teshima, Y. Shirai, and T. Miyasaka, “Organometal halide perovskites as visible-light sensitizers for photovoltaic cells,” *J Am Chem Soc*, vol. 131, no. 17, pp. 6050–6051, May 2009, doi: 10.1021/ja809598r.

[28] M. M. Lee, J. Teuscher, T. Miyasaka, and H. J. Snaith, “Efficient Hybrid Solar Cells Basedon Meso-Superstructured Organometal Halide Perovskites,” *Science (1979)*, vol. 338, no. 6107, pp. 640–643, Nov. 2012, doi: 10.1126/science.1227193.

[29] H. S. Kim *et al.*, “Lead iodide perovskite sensitized all-solid-state submicron thin film mesoscopic solar cell with efficiency exceeding 9%,” *Scientific Reports*, vol. 2, 2012, doi: 10.1038/srep00591.

[30] H. Min *et al.*, “Perovskite solar cells with atomically coherent interlayers on SnO2 electrodes,” *Nature*, vol. 598, no. 7881, pp. 444–450, Oct. 2021, doi: 10.1038/s41586-021-03964-8.

[31] National Renewable Energy Laboratory (NREL), “Best Research-Cell Efficiency Chart.” https://www.nrel.gov/pv/cell-efficiency.html (accessed Mar. 09, 2022).

[32] C. Zuo *et al.*, “Self-Assembled 2D Perovskite Layers for Efficient Printable Solar Cells,” *Advanced Energy Materials*, vol. 9, no. 4, Jan. 2019, doi: 10.1002/aenm.201803258.

[33] D. S. Ham *et al.*, “Influence of Drying Conditions on Device Performances of Antisolvent-Assisted Roll-To-Roll Slot Die-Coated Perovskite Solar Cells,” *ACS Applied Energy Materials*, vol. 4, no. 8, pp. 7611–7621, Aug. 2021, doi: 10.1021/acsaem.1c00892.

[34] J. Li *et al.*, “20.8% Slot-Die Coated MAPbI3 Perovskite Solar Cells by Optimal DMSO-Content and Age of 2-ME Based Precursor Inks,” *Advanced Energy Materials*, vol. 11, no. 10, Mar. 2021, doi: 10.1002/aenm.202003460.

[35] C. Li *et al.*, “Monoammonium Porphyrin for Blade-Coating Stable Large-Area Perovskite Solar Cells with >18% Efficiency,” *J Am Chem Soc*, vol. 141, no. 15, pp. 6345–6351, Apr. 2019, doi: 10.1021/jacs.9b01305.

[36] P. Li *et al.*, “Inkjet manipulated homogeneous large size perovskite grains for efficient and large-area perovskite solar cells,” *Nano Energy*, vol. 46, pp. 203–211, Apr. 2018, doi: 10.1016/j.nanoen.2018.01.049.

[37] L. Zhang *et al.*, "Ambient Inkjet-Printed High-Efficiency Perovskite Solar Cells: Manipulating the Spreading and Crystallization Behaviors of Picoliter Perovskite Droplets," *Solar RRL*, vol. 5, no. 5, May 2021, doi: 10.1002/solr.202100106.

[38] Saule Technologies, "Our Products." https://sauletech.com/product/ (accessed Mar. 12, 2022).

[39] B. Yang *et al.*, "Observation of Nanoscale Morphological and Structural Degradation in Perovskite Solar Cells by in Situ TEM," *ACS Applied Materials and Interfaces*, vol. 8, no. 47, pp. 32333–32340, Nov. 2016, doi: 10.1021/acsami.6b11341.

[40] S. Kundu and T. L. Kelly, "In situ studies of the degradation mechanisms of perovskite solar cells," *EcoMat*, vol. 2, no. 2, Jun. 2020, doi: 10.1002/eom2.12025.

[41] G. Divitini *et al.*, "In situ observation of heat-induced degradation of perovskite solar cells," in *European Microscopy Congress 2016: Proceedings*, 2016. doi: 10.1002/9783527808465.emc2016.5355.

[42] Z. Li, M. Yang, J. S. Park, S. H. Wei, J. J. Berry, and K. Zhu, "Stabilizing Perovskite Structures by Tuning Tolerance Factor: Formation of Formamidinium and Cesium Lead Iodide Solid-State Alloys," *Chemistry of Materials*, vol. 28, no. 1, pp. 284–292, Jan. 2016, doi: 10.1021/acs.chemmater.5b04107.

[43] M. J. Hong, R. Y. Johnson, and J. G. Labram, "Impact of Moisture on Mobility in Methylammonium Lead Iodide and Formamidinium Lead Iodide," *Journal of Physical Chemistry Letters*, vol. 11, no. 13, pp. 4976–4983, Jul. 2020, doi: 10.1021/acs.jpclett.0c01369.

[44] J. Chung *et al.*, "Record-efficiency flexible perovskite solar cell and module enabled by a porous-planar structure as an electron transport layer," *Energy and Environmental Science*, vol. 13, no. 12, pp. 4854–4861, Dec. 2020, doi: 10.1039/d0ee02164d.

[45] M. Park *et al.*, "Mechanically Recoverable and Highly Efficient Perovskite Solar Cells: Investigation of Intrinsic Flexibility of Organic-Inorganic Perovskite," *Advanced Energy Materials*, vol. 5, no. 22, Nov. 2015, doi: 10.1002/aenm.201501406.

[46] A. Al-Ashouri *et al.*, "Monolithic perovskite/silicon tandem solar cell with >29% efficiency by enhanced hole extraction." [Online]. Available: https://www.science.org

[47] D. Yang *et al.*, "28.3%-efficiency perovskite/silicon tandem solar cell by optimal transparent electrode for high efficient semitransparent top cell," *Nano Energy*, vol. 84, Jun. 2021, doi: 10.1016/j.nanoen.2021.105934.

[48] S. Hoath, *Fundamentals of Inkjet Printing: The Science of Inkjet and Droplets*, 1st ed. Weinheim: Wiley-VCH, 2016.

[49] Z. Wei, H. Chen, K. Yan, and S. Yang, "Inkjet printing and instant chemical transformation of a CH3NH3PbI3/nanocarbon electrode and interface for planar perovskite solar cells,"

Angewandte Chemie - International Edition, vol. 53, no. 48, pp. 13239–13243, Nov. 2014, doi: 10.1002/anie.201408638.

[50] G. H. McKinley and M. Renardy, "Wolfgang von Ohnesorge," *Physics of Fluids*, vol. 23, no. 12, 2011, doi: 10.1063/1.3663616.

[51] Y. Bai *et al.*, "A pure and stable intermediate phase is key to growing aligned and vertically monolithic perovskite crystals for efficient PIN planar perovskite solar cells with high processibility and stability," *Nano Energy*, vol. 34, pp. 58–68, Apr. 2017, doi: 10.1016/j.nanoen.2017.02.019.

[52] N. Ahn, D. Y. Son, I. H. Jang, S. M. Kang, M. Choi, and N. G. Park, "Highly Reproducible Perovskite Solar Cells with Average Efficiency of 18.3% and Best Efficiency of 19.7% Fabricated via Lewis Base Adduct of Lead(II) Iodide," *J Am Chem Soc*, vol. 137, no. 27, pp. 8696–8699, Jul. 2015, doi: 10.1021/jacs.5b04930.

[53] N. J. Jeon, J. H. Noh, Y. C. Kim, W. S. Yang, S. Ryu, and S. il Seok, "Solvent engineering for high-performance inorganic-organic hybrid perovskite solar cells," *Nature Materials*, vol. 13, no. 9, pp. 897–903, 2014, doi: 10.1038/nmat4014.

[54] J. Cao *et al.*, "Identifying the Molecular Structures of Intermediates for Optimizing the Fabrication of High-Quality Perovskite Films," *J Am Chem Soc*, vol. 138, no. 31, pp. 9919–9926, Aug. 2016, doi: 10.1021/jacs.6b04924.

[55] Y. Rong *et al.*, "Solvent engineering towards controlled grain growth in perovskite planar heterojunction solar cells," *Nanoscale*, vol. 7, no. 24, pp. 10595–10599, Jun. 2015, doi: 10.1039/c5nr02866c.

[56] Y. Yao *et al.*, "Impact of delay time before annealing MAI-PbI 2 -DMSO intermediate phase on perovskite film quality and photo-physical properties," *Crystals (Basel)*, vol. 9, no. 3, Mar. 2019, doi: 10.3390/cryst9030151.

[57] L. Zeng, S. Chen, K. Forberich, C. J. Brabec, Y. Mai, and F. Guo, "Controlling the crystallization dynamics of photovoltaic perovskite layers on larger-area coatings," *Energy and Environmental Science*, vol. 13, no. 12. Royal Society of Chemistry, pp. 4666–4690, Dec. 01, 2020. doi: 10.1039/d0ee02575e.

[58] M. Xiao *et al.*, "A fast deposition-crystallization procedure for highly efficient lead iodide perovskite thin-film solar cells," *Angewandte Chemie - International Edition*, vol. 53, no. 37, pp. 9898–9903, Sep. 2014, doi: 10.1002/anie.201405334.

[59] K. F. Lin *et al.*, "Unraveling the high performance of tri-iodide perovskite absorber based photovoltaics with a non-polar solvent washing treatment," *Solar Energy Materials and Solar Cells*, vol. 141, pp. 309–314, Jun. 2015, doi: 10.1016/j.solmat.2015.06.002.

[60] G. Jang, H. C. Kwon, S. Ma, S. C. Yun, H. Yang, and J. Moon, "Cold Antisolvent Bathing Derived Highly Efficient Large-Area Perovskite Solar Cells," *Advanced Energy Materials*, vol. 9, no. 36, Sep. 2019, doi: 10.1002/aenm.201901719.

[61] K. Liao *et al.*, “Hot-Casting Large-Grain Perovskite Film for Efficient Solar Cells: Film Formation and Device Performance,” *Nano-Micro Letters*, vol. 12, no. 1. Springer, Jul. 01, 2020. doi: 10.1007/s40820-020-00494-2.

[62] J. Li *et al.*, “Phase Transition Control for High-Performance Blade-Coated Perovskite Solar Cells,” *Joule*, vol. 2, no. 7, pp. 1313–1330, Jul. 2018, doi: 10.1016/j.joule.2018.04.011.

[63] H. Xiong *et al.*, “Modifying Perovskite Films with Polyvinylpyrrolidone for Ambient-Air-Stable Highly Bendable Solar Cells,” *ACS Applied Materials and Interfaces*, vol. 10, no. 41, pp. 35385–35394, Oct. 2018, doi: 10.1021/acsami.8b04236.

[64] B. Chaudhary *et al.*, “Poly(4-Vinylpyridine)-Based Interfacial Passivation to Enhance Voltage and Moisture Stability of Lead Halide Perovskite Solar Cells,” *ChemSusChem*, vol. 10, no. 11, pp. 2473–2479, Jun. 2017, doi: 10.1002/cssc.201700271.

[65] T. Ungár, “Microstructural parameters from X-ray diffraction peak broadening,” *Scripta Materialia*, vol. 51, no. 8 SPEC. ISS., pp. 777–781, 2004, doi: 10.1016/j.scriptamat.2004.05.007.

[66] C. F. Holder and R. E. Schaak, “Tutorial on Powder X-ray Diffraction for Characterizing Nanoscale Materials,” *ACS Nano*, vol. 13, no. 7. American Chemical Society, pp. 7359–7365, Jul. 23, 2019. doi: 10.1021/acsnano.9b05157.

[67] H. Xiong *et al.*, “Modifying Perovskite Films with Polyvinylpyrrolidone for Ambient-Air-Stable Highly Bendable Solar Cells,” *ACS Applied Materials and Interfaces*, vol. 10, no. 41, pp. 35385–35394, Oct. 2018, doi: 10.1021/acsami.8b04236.